

Impact of Rossby Wave Breaking on U.S. West Coast Winter Precipitation during ENSO Events

JU-MEE RYOO,* YOHAI KASPI,⁺ DARRYN W. WAUGH,[#] GEORGE N. KILADIS,[@]
DUANE E. WALISER,[&] ERIC J. FETZER,^{**} AND JINWON KIM⁺⁺

* Department of Earth and Planetary Sciences, University of California, Berkeley, Berkeley, California

⁺ Department of Environmental Sciences and Energy Research, Weizmann Institute of Science, Rehovot, Israel

[#] Department of Earth and Planetary Sciences, The Johns Hopkins University, Baltimore, Maryland

[@] Physical Sciences Division, NOAA/Earth System Research Laboratory, Boulder, Colorado

[&] Jet Propulsion Laboratory, California Institute of Technology, Pasadena, and Joint Institute for Regional Earth System Science and Engineering/Department of Atmospheric and Oceanic Sciences, University of California, Los Angeles, Los Angeles, California

^{**} Jet Propulsion Laboratory, California Institute of Technology, Pasadena, California

⁺⁺ Joint Institute for Regional Earth System Science and Engineering/Department of Atmospheric and Oceanic Sciences, University of California, Los Angeles, Los Angeles, California

(Manuscript received 22 May 2012, in final form 24 February 2013)

ABSTRACT

This study demonstrates that water vapor transport and precipitation are largely modulated by the intensity of the subtropical jet, transient eddies, and the location of wave breaking events during the different phases of ENSO. Clear differences are found in the potential vorticity (PV), meteorological fields, and trajectory pathways between the two different phases. Rossby wave breaking events have cyclonic and anticyclonic regimes, with associated differences in the frequency of occurrence and the dynamic response. During La Niña, there is a relatively weak subtropical jet allowing PV to intrude into lower latitudes over the western United States. This induces a large amount of moisture transport inland ahead of the PV intrusions, as well as northward transport to the west of a surface anticyclone. During El Niño, the subtropical jet is relatively strong and is associated with an enhanced cyclonic wave breaking. This is accompanied by a time-mean surface cyclone, which brings zonal moisture transport to the western United States. In both (El Niño and La Niña) phases, there is a high correlation ($>0.3\text{--}0.7$) between upper-level PV at 250 hPa and precipitation over the west coast of the United States with a time lag of 0–1 days. Vertically integrated water vapor fluxes during El Niño are up to $70 \text{ kg m}^{-1} \text{ s}^{-1}$ larger than those during La Niña along the west coast of the United States. The zonal and meridional moist static energy flux resembles wave vapor transport patterns, suggesting that they are closely controlled by the large-scale flows and location of wave breaking events during the different phase of ENSO.

1. Introduction

The El Niño–Southern Oscillation (ENSO) is a quasiperiodic large-scale climate pattern in the tropical Pacific Ocean, characterized by large sea surface temperature variations in the tropical eastern Pacific on interannual time scales with a period ranging from 2 to 7 yr (e.g., Diaz and Markgraf 1992; Tziperman et al. 1994; Changnon 2000). An interesting feature of ENSO

is that although ENSO is the dominant interannual oscillation pattern in the tropics, its impact also extends to the time-mean subtropical and extratropical atmospheric circulation. Bjerknes (1969) showed that an anomalous heat source from tropical deep convection changes the Hadley circulation and thus strongly influences the strength and the location of the subtropical upper-level jet. This influence is realized in both hemispheres, but a stronger response appears in the winter hemisphere. In the extratropics, ENSO is associated with zonally asymmetric wavelike anomalies extending from subtropics to the mid to high latitudes of both hemispheres (Karoly 1989; Seager et al. 2003; L'Heureux and Thompson 2005).

Corresponding author address: Ju-Mee Ryoo, Department of Earth and Planetary Sciences, University of California, Berkeley, Berkeley, CA 94720.
E-mail: jryoo@berkeley.edu

In addition, ENSO's influence over large regions often culminates in extreme weather. Renwick and Wallace (1996) demonstrated the impact of ENSO on atmospheric blocking events over the North Pacific, showing that the frequency of blocking episodes tends to decrease during El Niño. Bradley et al. (1987) showed that ENSO is highly related to continental precipitation. Precipitation along the west coast of the United States is impacted by ENSO during winter, with El Niño years favoring higher than normal precipitation over the southwest United States, and drier conditions over the Pacific Northwest (e.g., Mo and Higgins 1998; Schubert et al. 2008), with the location of precipitation varying due to the alteration of the Pacific storm track.

Baroclinic Rossby waves, also known as planetary waves, are long horizontal wavelength (>2000 km) oscillations in the westerlies that predominantly occur in the upper troposphere and the lower stratosphere. In the Northern Hemisphere (NH) winter, Rossby waves can grow to large amplitudes and eventually break with irreversible mixing of potential vorticity. Some idealized studies showed that these waves are strongly related to baroclinic wave life cycles (Davies et al. 1991; Thorncroft et al. 1993; Shapiro et al. 1999). Davies et al. (1991) distinguished three different classes: nonshear, anticyclonic, and cyclonic shear cases within a baroclinic flow surface synoptic development. Thorncroft et al. (1993) found that two distinct types of Rossby wave breaking occur at the end of baroclinic wave life cycles, and referred to them as life cycle 1 (LC1) and life cycle 2 (LC2). They also showed that LC1 ends with an anticyclonic wave breaking, and LC2 ends with a cyclonic wave breaking; anticyclonic wave breaking features a narrow tongue tilted in the southwestward and equatorward direction, and cyclonic wave breaking is characterized by a broad trough tilting in the northwestward and the poleward direction. Martius et al. (2007) classified a neutral (LC1) and an anticyclonic life cycle (LC3) that both exhibit a similar upper-level potential vorticity (PV) evolution, and therefore they combined these types as LC1 without any distinction between them. Shapiro et al. (2001) selected LC1 versus LC2 events in a manner similar to the above studies, but LC1 was identified as those with PV maxima oriented southwest to northeast that extended into the subtropics, while LC2 was identified as having zero to negative tilts in PV maxima. Anticyclonic Rossby wave breaking events often bring air with high PV into the subtropics (Webster and Holton 1982; Kiladis and Weickmann 1992; Hoskins and Ambrizzi 1993; Waugh et al. 1994); they are also referred to as PV intrusions (Waugh and Polvani 2000; Waugh 2005).

Synoptic-scale weather and interannual variability are also closely related to Rossby wave breaking events

(Hoskins et al. 1985; Moore et al. 2010; Michel and Rivière 2011). Michel and Rivière (2011) showed that the transitions of weather regimes such as Greenland anticyclones, Atlantic ridges, zonal flows, and blocking events are closely linked to Rossby wave breaking events over the North Atlantic and Europe. In recent years, the relationship among upper-level PV intrusions into the subtropics, humidity, and convective clouds has been studied (Funatsu and Waugh 2008, Ryoo et al. 2008). Funatsu and Waugh (2008) showed that there is increased cloudiness, lower static stability, upward motion, and an increase of convective available potential energy (CAPE) at the leading edge of high PV intrusions. Ryoo et al. (2008) also showed that upper-level humidity during the Northern Hemisphere wintertime is controlled by PV intrusions over the eastern Pacific and Atlantic Ocean. Moore et al. (2010) found that LC2 waves associated with cyclonic Rossby wave breaking often accompanies cutoff surface cyclones at high latitudes, especially to the north of narrow jets. LC2 waves were reported to be closely linked to the formation of comma clouds (Carlson 1980). Waugh and Polvani (2000) investigated the mean flow in the different phases of ENSO and PV intrusions and found that PV intrusions seldom occur in the warm phase of ENSO. It has been reported that during El Niño years, the subtropical jet is observed to be displaced equatorward from its normal position (Rosen et al. 1984) together with associated high-frequency eddy activity. Orlanski (2005) showed that the anticyclonic (cyclonic) wave breaking creates a ridge (trough) in the eastern Pacific, and that the type of breaking is in part controlled by SST anomalies created by ENSO because of their direct influence on the low-level baroclinicity. Kiladis (1998) also demonstrated that there is substantial interannual variability of wave activity, which suggests that the wave activity is sensitive to the changes in the large-scale basic-state circulation and reorganization of transient activity through basic-state variations.

Although the impact of Rossby wave breaking on weather regimes and upper-level humidity has been studied, the role of PV intrusions in determining the characteristics and the patterns of landfalling precipitation during the different phases of ENSO is not yet fully understood. Enhanced water vapor bands making landfall along the west coast of North America, termed atmospheric rivers (ARs; Ralph et al. 2004, 2006; Neiman et al. 2008), are often observed along relatively narrow regions within the warm conveyor belt associated with a cold front. Note that the characteristic patterns in a developing baroclinic system are ascending motion of warm surface air near the warm conveyor belt, along with descending motion in the dry intrusion from

the upper level (Polvani and Esler 2007). The lower level is highly coupled with the upper-level disturbance in a developing baroclinic system, and the nature of this coupling has substantial interannual variability related to the frequency of each wave breaking type. Therefore, this suggests that understanding the patterns and frequency of wave breaking events during different phases of ENSO may help to understand the location and intensity of heavy precipitation events such as ARs. There have been several studies that looked at the relationship of ENSO phase to heavy precipitation. Andrews et al. (2003) showed that south of 35°N along the California coast, floods are notably larger during an El Niño phase than a non–El Niño phase. While characterizing the ARs during 1998 El Niño winter and 2001 La Niña winter, Ralph et al. (2005) showed that the northward moisture transport toward California's coastal mountains is larger during El Niño winter and therefore may also contribute to greater orographic precipitation enhancement during the warm phase of ENSO.

The primary goal of this study is to understand the characteristics and controls of the precipitation over the west coast of the United States associated with upper-level Rossby wave breaking in different ENSO phases during NH winters [December–February (DJF)]. For this purpose, we contrast the flow and moisture flux between four El Niño (1982/83, 1997/98, 2002/03, 2009/10) and four La Niña (1998/99, 2000/01, 2007/08, 2008/09) years. Hereinafter in the text and captions, these two groups will be referred to as the four El Niño and the four La Niña years. The data and trajectory model configuration used in this study are described in section 2. In section 3, the meteorological fields and trajectory patterns during the different period of ENSO are illustrated. Then we proceed to demonstrate the correlation between PV and precipitation, and the role of the transient eddies on the time-mean flow and the water vapor transports in terms of latent heating and moist static energy in sections 4 and 5, respectively. In section 6, the conclusions and future work are discussed.

2. Data and methods

We examine the flow, moisture transport, and precipitation for the four El Niño and the four La Niña years. These winters were chosen based on the Southern Oscillation index (SOI), with an index larger (smaller) than +0.5 (−0.5) during DJF categorized as a La Niña (El Niño) winter. No difference is found when we utilize the oceanic Niño index (ONI) in identifying ENSO events. In most of the analysis below we present composite-mean fields averaged over the four El Niño or four La Niña winters.

In our analysis we use temperature, wind, geopotential height, potential vorticity, specific humidity, and relative humidity (RH) fields from the National Aeronautics and Space Administration (NASA) Modern-Era Retrospective Analysis for Research and Applications (MERRA) reanalysis data (Suarez 2008; Bosilovich et al. 2008, 2011). The precipitation data used are acquired from the National Centers for Environmental Prediction (NCEP) and the Climate Prediction Center $0.25^\circ \times 0.25^\circ$ gridded daily rain gauge analysis (Higgins et al. 2000). The water vapor, temperature, and geopotential height from MERRA are compared with those from the Atmospheric Infrared Sounder Satellite (AIRS; Aumann et al. 2003; Fetzer et al. 2003) data, and they are consistent with each other in terms of patterns and magnitude except for the missing data period of 10–25 January 2010 (not shown).

The trajectory calculations in this study are performed using the NASA Goddard quasi-isentropic trajectory model (Schoeberl and Sparling 1995; Wright et al. 2011). For a given velocity $U(t)$, the parcel history (back trajectory) $X(t)$ is calculated from $DX(t)/Dt = U(t)$, where $X(t)$ is a function of longitude, latitude, and potential temperature. Trajectory vertical motion is obtained by computing the change in the potential temperature as a function of time, $D\theta/Dt$. This $D\theta/Dt$ is determined by $Q(p_s/p)^k$, where, Q is a total diabatic heating rate, P (P_s) is a pressure (surface pressure), and k is R/C_p , where R is the gas constant and C_p is a specific heat capacity at constant pressure (Yanai et al. 1973). The trajectory calculations were performed using the fourth-order Runge–Kutta method with a 28-min time step. We utilize 6-hourly winds and temperature from MERRA to determine the parcel trajectories. The horizontal resolution of MERRA is $0.66^\circ \times 0.5^\circ$ ($1.25^\circ \times 1.25^\circ$ for some fields including specific and relative humidity) with 42 vertical pressure levels ranging from 1000 hPa up to 0.01 hPa. They are diagnosed using both the model and assimilation and strongly reflect the observational data. For resolving vertical motion, MERRA heating rates are used. Three-hourly diabatic heating rates are used with reduced horizontal resolution ($1.25^\circ \times 1.25^\circ$). They are regridded in time to match the spatial and temporal resolution of wind and temperature obtained from MERRA. This includes shortwave and longwave radiation, latent heat release due to water vapor condensation, surface sensible heat flux, gravity wave dissipation, vertical diffusion of temperature in the PBL, and frictional dissipation. Since the trajectory vertical motion is determined by the diabatic heating, the process of convective heating is implicitly included while a parcel is being advected.

Tests using meteorological fields from NCEP (Kalnay et al. 1996), MERRA, or ECMWF (Simmons et al. 2007)

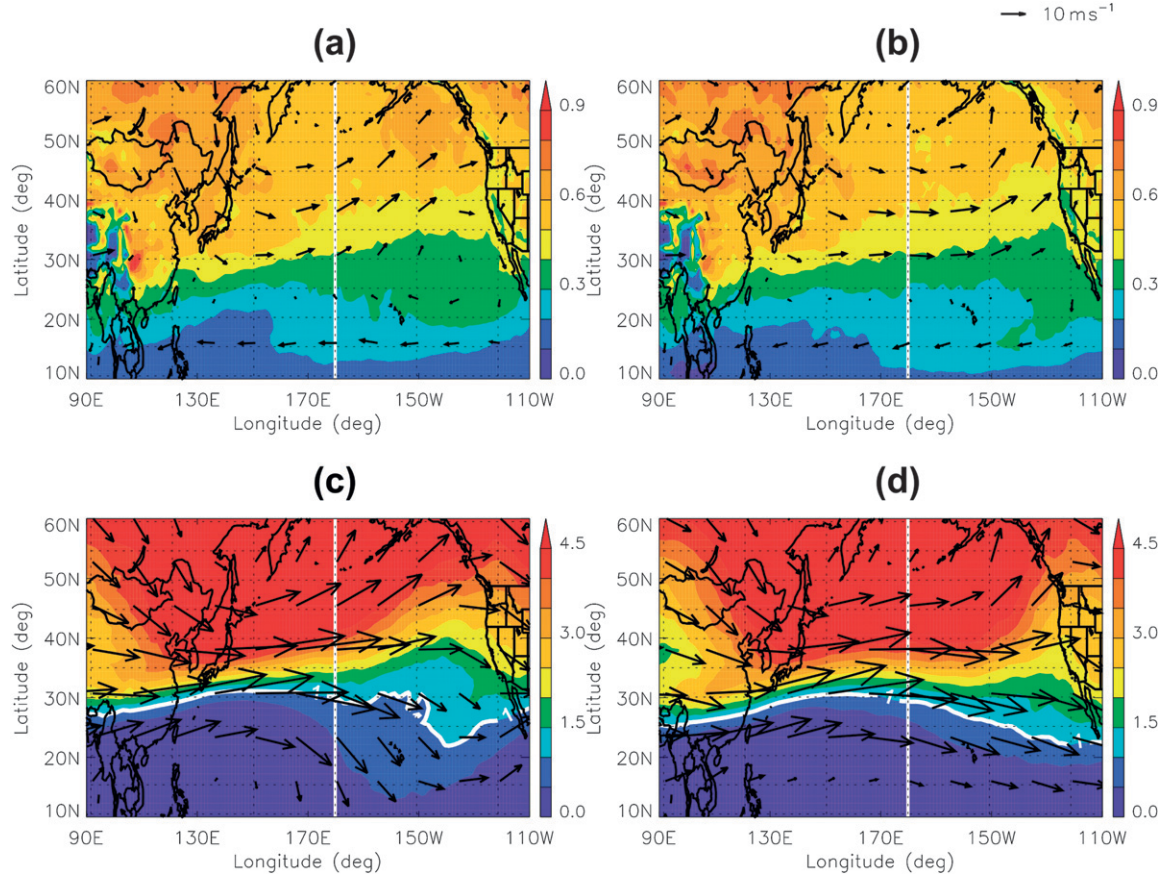


FIG. 1. Longitude–latitude cross section of Ertel's PV (shading; PVU) and winds (arrows; m s^{-1}) at (a),(b) 850 and (c),(d) 250 hPa during NH winter (DJF) in (left) the four La Niña and (right) the four El Niño years. The white curves are PV = 1 PVU ($=10^{-6} \text{ K m}^2 \text{ kg}^{-1} \text{ s}^{-1}$).

show no significant differences for trajectories in our region of interest (Ryoo et al. 2010). Furthermore, there is good agreement between trajectories from our model and from the National Oceanic and Atmospheric Administration Air Resources Laboratory Hybrid Single-Particle Lagrangian Integrated Trajectory (HYSPLIT) model (see <http://ready.arl.noaa.gov/HYSPLIT.php>) for several extreme precipitation events (e.g., AR events).

3. Meteorological conditions

a. Climatology of PV and meteorological fields

Figures 1a and 1b show composite mean PV and horizontal winds during the four El Niño and the four La Niña years. During La Niña, the jet is weaker than normal and shifted to the north with an anticyclonic pattern near the west coast of the United States at 850 hPa. At 250 hPa, the jet also becomes weak in the central Pacific with a signature of a strong PV intrusion around 170°E–170°W and 150°–130°W in the subtropics ($\sim 25^\circ\text{N}$). In contrast, during El Niño at 850 hPa, the jet

maximum extends to the east with a surface cyclone on the northern flank of the strong jet. At 250 hPa, the strong jet prevails over the Pacific with a strong PV gradient aloft. The mean geopotential height and zonal winds at 850 and 250 hPa and the departures from the zonal mean are shown in Fig. 2. At both levels, the mean and anomaly fields show that geopotential height is higher in the eastern Pacific with a strong Aleutian low over the central-north Pacific with weak zonal winds during La Niña, whereas it is lower and more zonally extended over the eastern Pacific under the existence of a strong jet during El Niño.

Figure 3 shows water vapor at lower (850 hPa) and upper (250 hPa) levels, and 2-m temperature for La Niña and El Niño. As shown in Fig. 1, during La Niña a strong jet developed over the western Pacific (30° – 35°N , 120° – 140°E) and spread out into the northern and southern branches of the flows at the jet exit region (25° – 35°N , 180°). Soon after passing over the jet exit region, the southern branch of the flow merges with the poleward flow from the tropics (10° – 20°N , 170° – 150°W and 130° – 110°W) and brings high moisture to the North Pacific

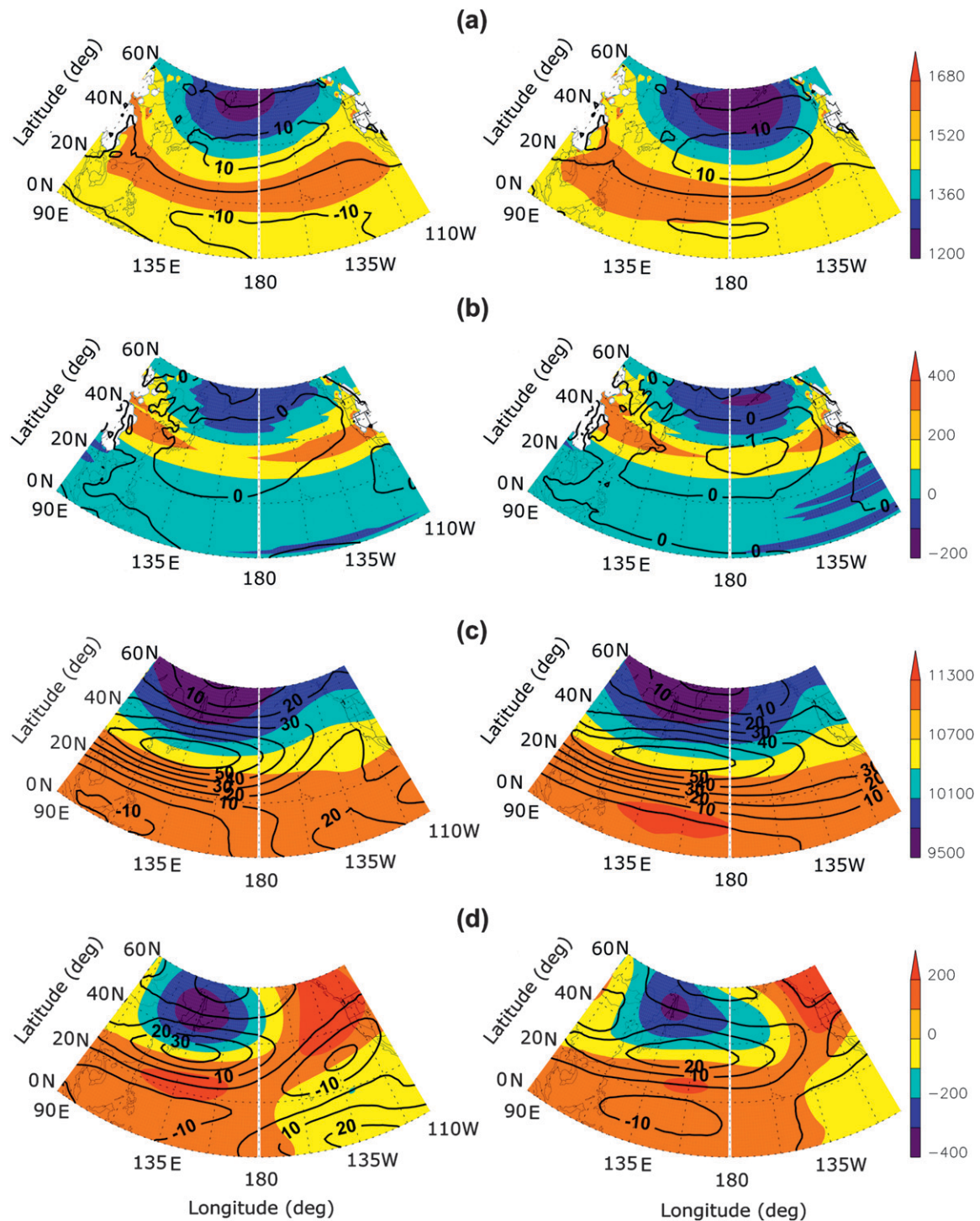


FIG. 2. The NH winter (DJF) longitude–latitude cross sections of (a) mean and (b) departures from the mean of geopotential heights (shading; m) and zonal winds (contours; $m s^{-1}$) at 850 hPa in (left) the four La Niña and (right) the four El Niño years. (c),(d) As in (a),(b), but for 250 hPa. The white blank areas in (a) and (b) are mountain regions where missing data exist in reanalysis (e.g., the Himalayas and Rocky Mountains). The projection is Albers equal area, with standard parallels at 0° and $60^{\circ}N$.

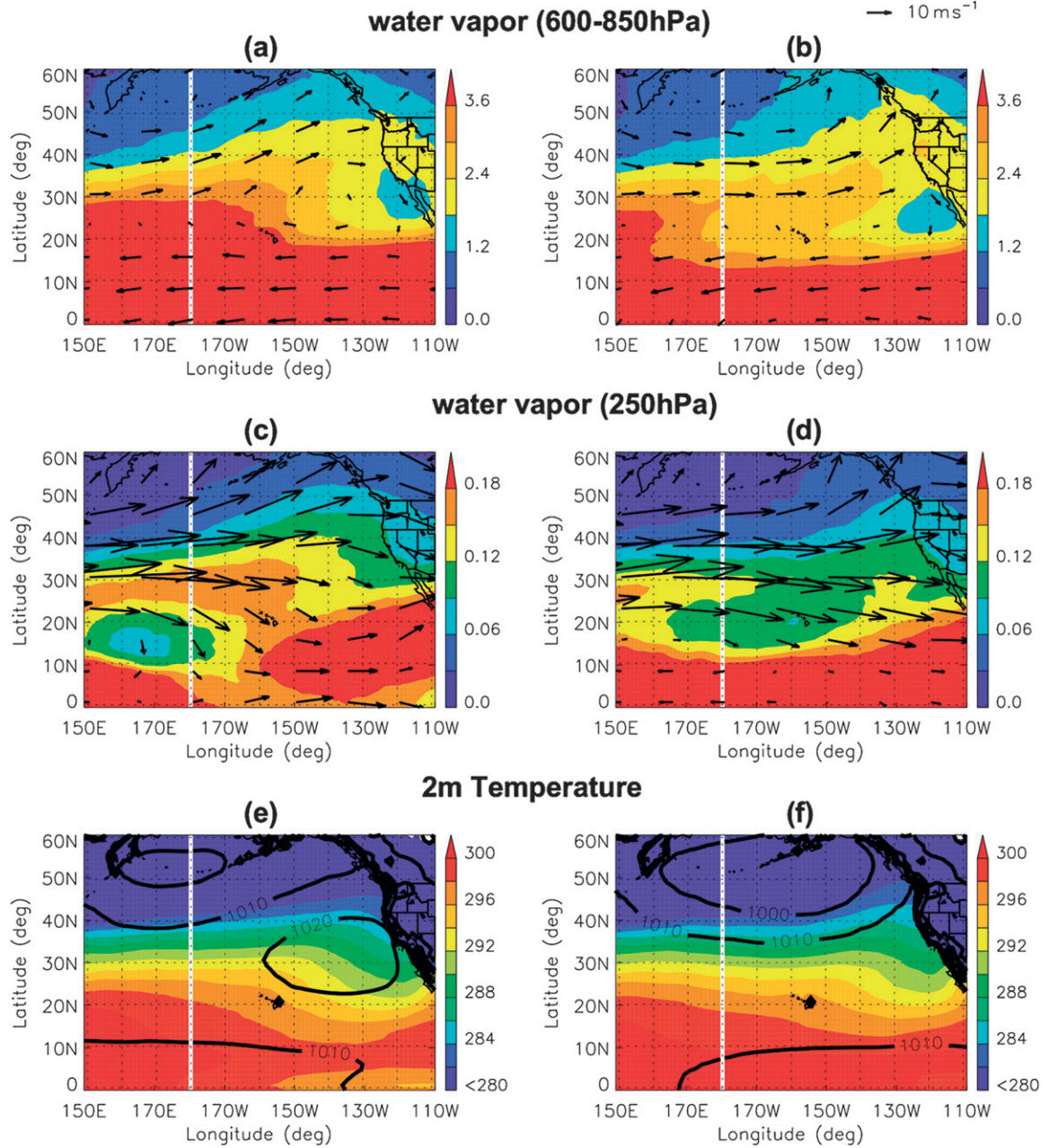


FIG. 3. The NH winter (DJF) longitude–latitude cross sections of water vapor (shading; g kg^{-1}) and winds (arrows; m s^{-1}) averaged over (a),(b) 600–850 and (c),(d) 250 hPa and of (e),(f) 2-m temperature (shading; K) and surface pressure (contours; hPa) in (left) the four La Niña and (right) the four El Niño years.

and the western United States (Fig. 3c). These northward flows shown in Fig. 3c are regarded as being induced by strong upper-level PV intrusions, carrying high moisture from the tropics into the subtropics. Since the moisture is most abundant near the surface, the high moisture transport from the surface associated with upper-level PV intrusion is seen more clearly in the region around $170^{\circ}\text{--}140^{\circ}\text{W}$ where a flow of moisture is

transported from the surface along the surface anticyclone (Fig. 3a). High moisture content at upper levels is also seen to the east (ahead) of the region where the PV intrusion occurs (Fig. 3c, around $130^{\circ}\text{--}110^{\circ}\text{W}$). During El Niño, no split of horizontal winds is detected over the entire Pacific basin (Figs. 1d and 3d). This single strong subtropical jet prohibits the injection of moisture from the tropics to the midlatitudes, so the direction of water

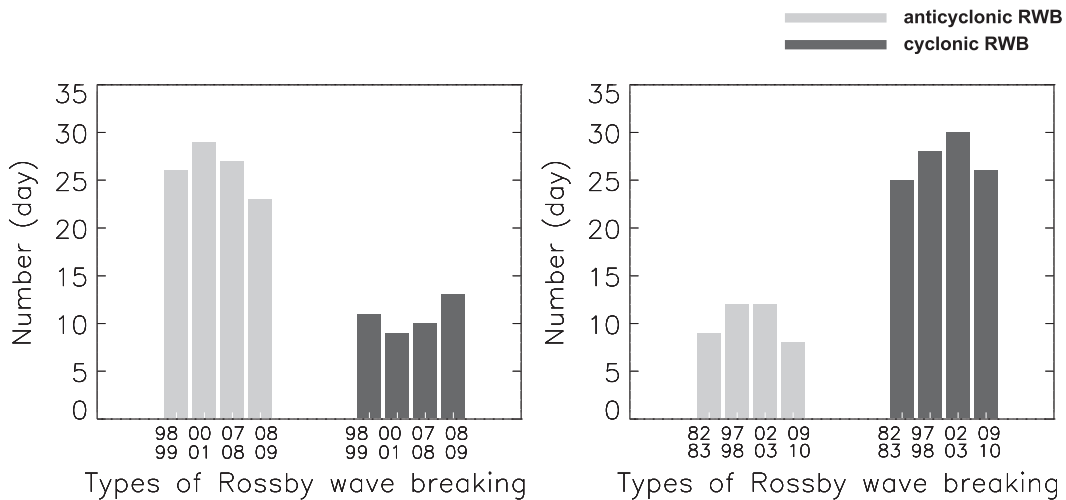


FIG. 4. The frequency of anticyclonic and cyclonic Rossby wave breaking (RWB) events during (left) La Niña (1998/99, 2000/01, 2007/08, and 2008/09) and (right) El Niño (1982/83, 1997/98, 2002/03, and 2009/10) years.

vapor transport becomes more zonally aligned toward the west coastal regions of the United States.

The 2-m temperature (Figs. 3e,f) is warmer during El Niño than La Niña in the tropical eastern Pacific, especially from the center of date line eastward extending to the South America. The 2-m air temperature is also warmer in the coastal regions of the North America during El Niño. For example, around 42°N and 125°W, 2-m temperature is 282–284 K in Fig. 3e but 284–286 K in Fig. 3f, which is about 2 K warmer than that in Fig. 3e. The difference is shown more clearly in the anomaly field (deviation from the climatological mean; not shown). During La Niña episodes, abnormally low surface pressure covers the tropical western Pacific and abnormally high air pressure covers the tropical eastern Pacific. In contrast, during El Niño, low surface pressure resides in the tropical eastern Pacific.

b. Rossby wave breaking events

Rossby wave breaking events are categorized into two types according to their orientation from their maximum. This is identified in a slightly different but similar manner to Waugh (2005) and Ryoo et al. (2008): All days where $PV \geq 2.5$ PVU¹ at 20°–50°N within 10° longitude from the central-eastern Pacific region (140°E–110°W) were identified. If the orientation from the PV maximum is northeast–southwestward, then it is called an anticyclonic

Rossby wave breaking event, and if the orientation from the PV maximum is northwest–southeastward, then it is called a cyclonic Rossby wave breaking event. An occurrence on a given day is counted as a single event.

Figure 4 shows the frequency of anticyclonic and cyclonic Rossby wave breaking events in the central-eastern Pacific (140°E–110°W). During La Niña the number of anticyclonic wave breaking events is higher compared to that of cyclonic wave breaking events (104 anticyclonic wave breaking events and 53 cyclonic wave events), while cyclonic wave breaking events occur more often during El Niño (41 anticyclonic wave breaking events and 108 cyclonic wave breaking events). This difference in relative frequency of anticyclonic and cyclonic wave breaking between La Niña and El Niño winters is consistent with the previous studies. Shapiro et al. (2001) suggested that anomalies in the time-mean environmental flow associated with 1997/99 ENSO lead to preferential baroclinic life cycles over the eastern North Pacific that closely resemble the LC1 and LC2 wave breaking for La Niña and El Niño winters, respectively. Also, Matthew and Kiladis (1999) reported that high-to-low latitude Rossby wave propagation is suppressed during El Niño, with less cross-equatorial propagation of wave activity during the 1997/98 El Niño, and Waugh and Polvani (2000) found that fewer PV intrusions into the subtropics (LC1-like anticyclonic wave breaking events) occur during the warm phase of ENSO.

To illustrate the difference in the flow during the different types of events, Fig. 5 shows examples of the PV at 250 hPa for two particular days: one during La Niña and the other during El Niño. Both cases are

¹Potential vorticity units (PVU) are the unit of PV, defined as $1 \text{ PVU} = 10^{-6} \text{ m}^2 \text{s}^{-1} \text{K kg}^{-1}$. Typically, values of PV less than 1.5 PVU are associated with tropospheric air and those greater than 1.5 PVU are associated with stratospheric air.

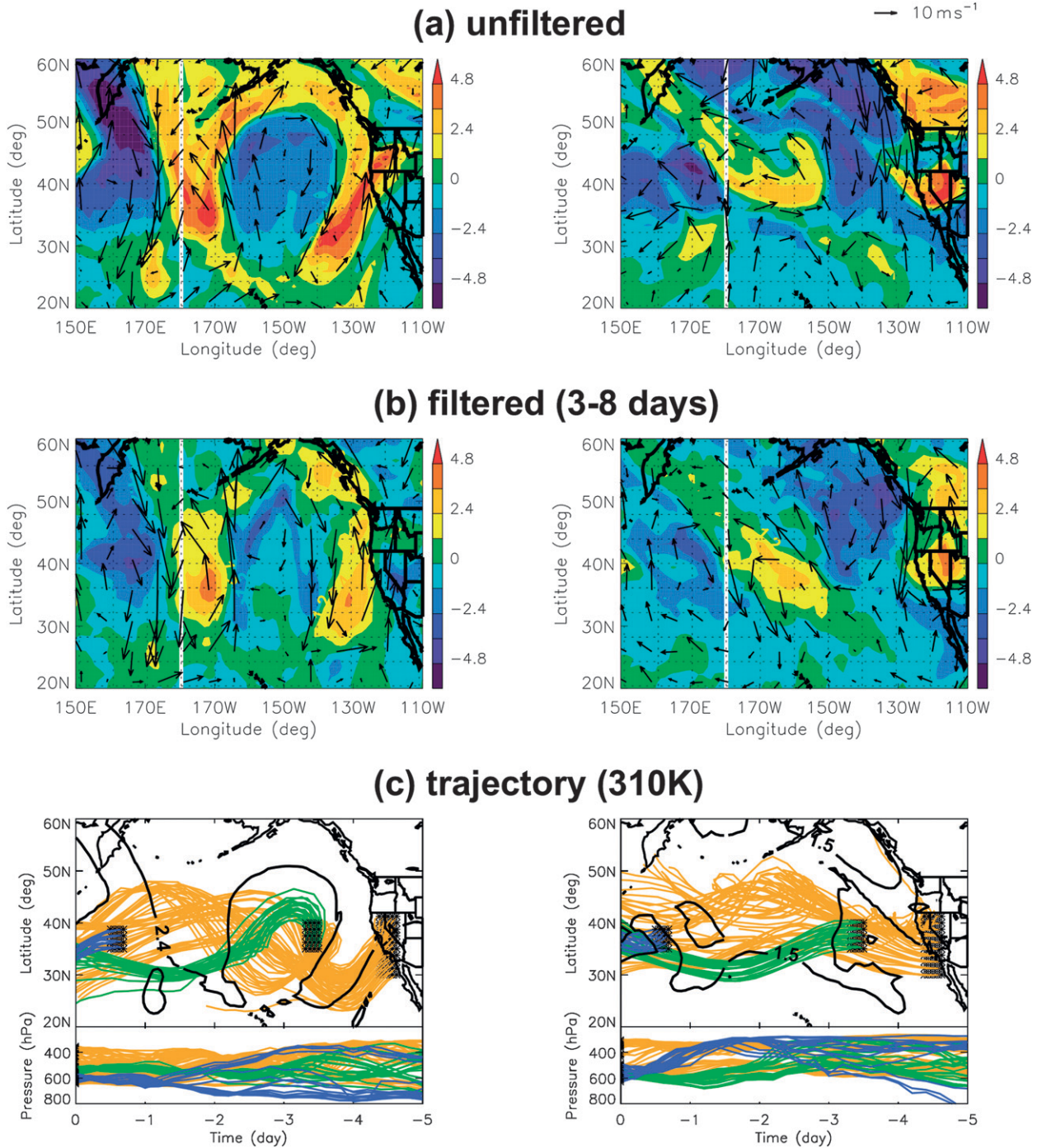


FIG. 5. (a) Unfiltered and (b) 3–8-day Lanczos bandpass filtered PV (shading; PVU) and horizontal winds anomalies subtracted from the seasonal mean (vector; m s^{-1}) at 250 hPa and (c) horizontal pathways (top part of panels) and vertical variations (bottom part of panels) of backward trajectories on the 310-K surface from the different ending points [marked by asterisks: $34^{\circ}\text{--}39^{\circ}\text{N}, 160^{\circ}\text{--}164^{\circ}\text{W}$ (blue); $34^{\circ}\text{--}41^{\circ}\text{N}, 144^{\circ}\text{--}140^{\circ}\text{W}$ (green); and $30^{\circ}\text{--}42^{\circ}\text{N}, 123^{\circ}\text{--}117^{\circ}\text{W}$ (orange)] for (left) 1200 UTC 24 Jan 2009 during La Niña and (right) 1200 UTC 13 Dec 2009 during El Niño. Time (day) = 0 is when trajectory starts to trace backward, and negative time means backward simulation.

related to heavy landfalling precipitation (e.g., an atmospheric river) over the west coast of the United States within ± 5 days from the marked day. Filtered PV and horizontal wind anomalies at 250 hPa are obtained from a 3–8-day Lanczos bandpass filter (Duchon 1979) to isolate the high-frequency component (3–8-day synoptic waves). Unfiltered PV fields in both cases resemble the synoptic wave patterns such as an anticyclonic baroclinic wave (LC1) and a cyclonic baroclinic wave (LC2), respectively. The anticyclonic PV intruding to the subtropics-midlatitudes is observed near the central-eastern Pacific and the western United States, which are similar to the LC1 wave signature. In contrast, a strong cyclonic PV pattern extending into the northern Pacific shows similarity to the LC2 wave pattern captured in the 3–8-day filtered data. This shows that the unfiltered PV fields themselves can well represent the motion of synoptic-scale waves.

c. Trajectory pathways

To find where air parcels (air masses) arriving at the west coast of the United States originate in the different phases of ENSO years, we performed trajectory simulations. Figure 5c shows the horizontal pathways and vertical variations of the backward trajectories on 310 K at the different ending points for the two illustrative wave breaking events. Trajectories look very different for these two events, and those differences are related to the location and type of the wave breaking events. These features are shown in the mean trajectories that end on the west coast of the United States. Figure 6 shows the mean trajectories simulated backward on the 300-K isentropic surface at the Sierra Nevada region (37.5°N , 120°W) in La Niña (Fig. 6a) and El Niño (Fig. 6b) years. Here we show the trajectories in the Sierra Nevada region because the high elevation of the Sierra Nevada exerts a major orographic forcing to moisture-rich inflows during winter storms, so that this mountain precipitation is of great practical importance to the western United States (Grubisic et al. 2005; Kim 1997; Soong and Kim 1996). In addition, snowpack accumulated in the high elevations provides a major water resource to California (Anderson et al. 2008). Trajectory patterns we found near the Sierra Nevada regions, which are northward during La Niña and are more zonal during El Niño, are also observed over the northern regions of the west coast of the United States such as Oregon and Washington (not shown).

Trajectories on the wave breaking events and the mean trajectories show different characteristics during the two ENSO phases, and they are associated with different origins and pathways. Clear differences appear to be governed by the different properties of ENSO.

Most of the trajectories ending at the west coast of the United States during La Niña are from the northeastern Pacific. During El Niño, air masses are directly transported from the western Pacific to the reference region without penetrating into the northeastern Pacific. More variability is found during La Niña than El Niño. These different pathways of trajectories are related to the strength of the subtropical jet (see Fig. 1), as well as the different transport processes associated with upper-level Rossby wave breaking. From the analysis of the large-scale flows, water vapor, and temperature patterns associated with the wave breaking events during ENSO, we will examine further how precipitation patterns will look like, and how different wave breaking events will contribute to cause the different types of precipitation patterns in the next section.

4. Correlation between upper-level PV and precipitation

Temporal variability

We have seen that different patterns of PV are associated with variations in the large-scale mean flow. The modulations of PV associated with upper-level wave breaking are closely related to the development of frontal systems, so their impacts on surface temperature and precipitation are of particular interest (Knippertz and Martin 2007). Figures 7a and 7b show the time series of PV and precipitation along the west coast of the United States (30° – 50°N , 130° – 110°W) for La Niña and El Niño, respectively. During La Niña, heavy precipitation occurs roughly at the same time as the occurrence of high PV. This is not true for the entire time series (e.g., 1 January 2011) but is valid for the most of dates. In contrast, during El Niño heavy precipitation occurs either simultaneously or within one day following high-PV events. These patterns are confined to not only large regions of the western United States, but also narrower regions near the Sierra Nevada (37° – 39°N , 121° – 119°W ; not shown).

Another way to quantify the relationship between changes in upper-level PV and in precipitation is to calculate cross correlations over time. Figure 8 shows time series of upper level PV, precipitation, and relative humidity. Figure 8a shows that during La Niña (El Niño) the maximum correlation between PV at 250 hPa and precipitation occurs at lag = 0 (lag = +1) day with a value up to 0.7. These correlations get lower as the time lag increases in both phases. In Fig. 3c, we have seen that the highest water vapor occurs to the east of high-PV tongues (25° – 40°N , 170° – 150°W and 10° – 30°N , 130° – 110°W , respectively) especially at the upper level (250 hPa), and so does the RH (not shown). As shown in Fig. 8a, a negative correlation between PV and RH at

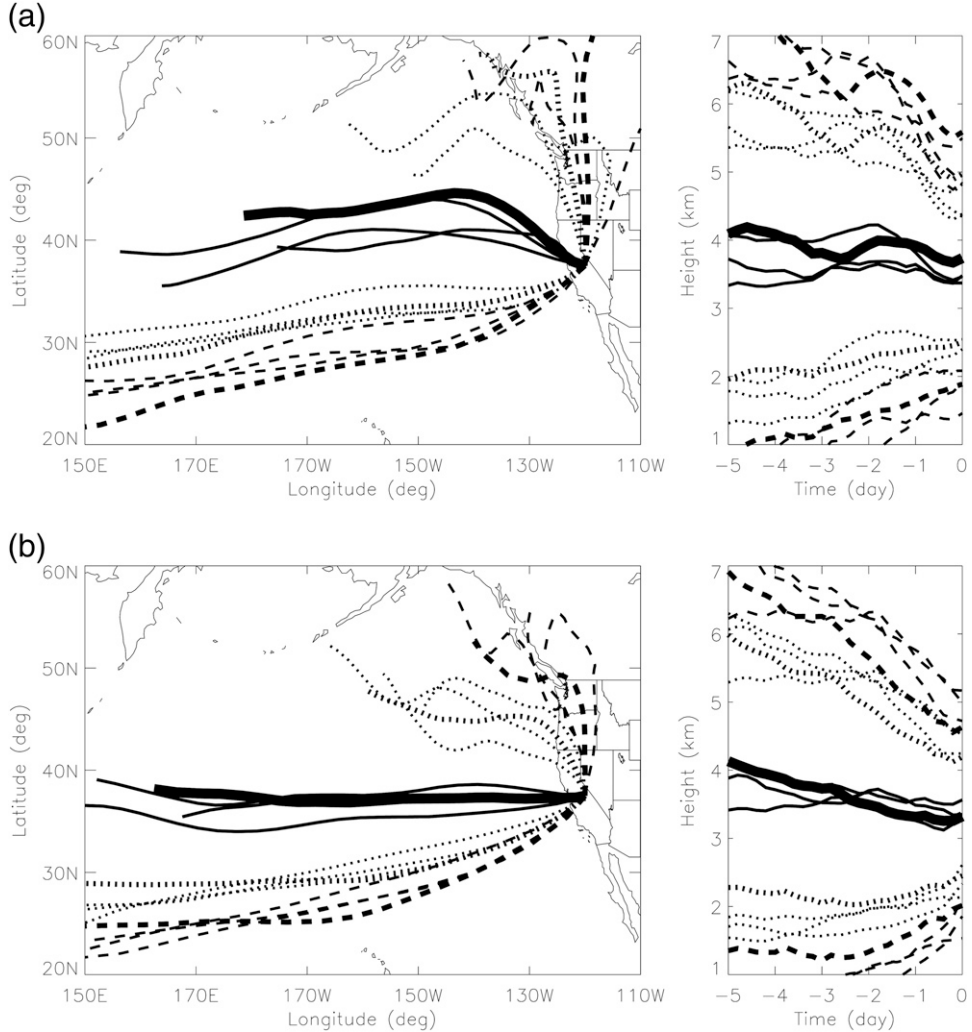


FIG. 6. (left) Longitude–latitude map of horizontal pathways and (right) vertical variations of backward trajectories on the 300-K surface at the Sierra Nevada (37.5°N , 120°W) from MERRA reanalysis data during NH winter (DJF) in (a) the four La Niña and (b) the four El Niño years. Solid lines represent the mean trajectories; dotted and dashed lines indicate ± 1 and ± 1.5 standard deviations from the mean trajectories, respectively. Mean trajectories are averaged over the days only if precipitation is $>1 \text{ mm day}^{-1}$. Time (day) = 0 is when trajectory starts to trace backward, and negative time means backward simulation.

250 hPa is observed over the west coast of the United States because high PV originates within dry and cold stratospheric air PV to the west of these tongues.

The fact that in both composites the correlation is high around lags from 0 to +1 day suggests that western U.S. precipitation is associated with the location and the time of presence of an upper-level PV aloft. Taking this fact into account, we compute the correlation between RH at a given longitude and PV 20° west of this longitude. Figure 8b shows that there is no clear correlation between PV shifted 20° west from a given longitude (30° – 45°N , 150° – 130°W) and precipitation (30° – 45°N , 130° – 110°W).

However, the correlation between PV at 250 hPa (20° – 35°N , 150° – 130°W) and RH at 250 hPa (20° – 35°N , 130° – 110°W) is relatively high in regions where PV often intrudes and anticyclonic wave breaking occurs at lag = 0 to +1 day, especially during La Niña. This is supported by the results of Waugh (2005) and Ryoo et al. (2008), showing that low RH at 250 hPa occurs west (behind) and within the high PV while high water vapor and RH throughout the whole atmosphere occur east (ahead) of high PV tongues. This can be due to convection, which tends to be induced on the east side of PV intrusions, as quantified by Funatsu and Waugh (2008). During La

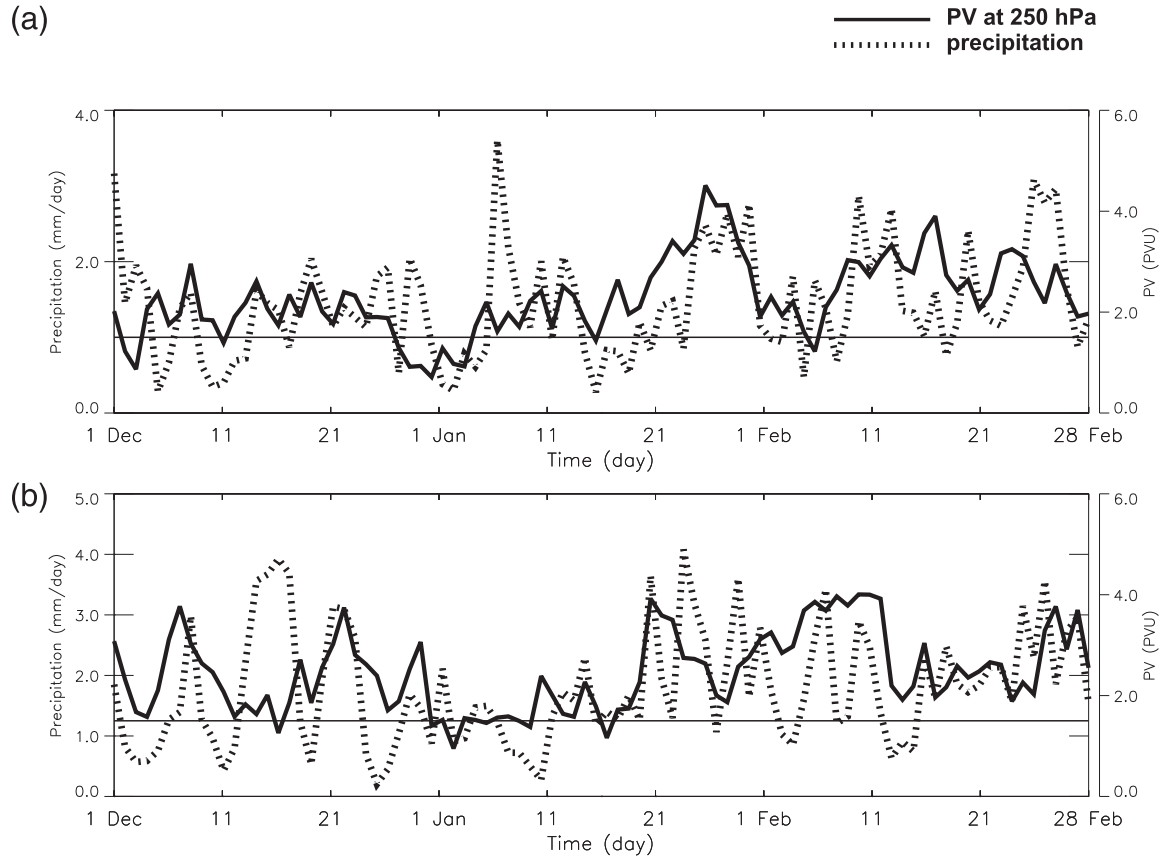


FIG. 7. Composite time series of PV at 250 hPa (thick solid line) and precipitation (dotted line) averaged over 30° – 45° N, 130° – 110° W during NH winter (DJF) in (a) the four La Niña and (b) the four El Niño years. The thin solid line indicates $PV = 1.5$ PVU.

Niña, the correlation is high in the northwestern United States, especially over Washington, Oregon, and Northern California, peaking its value at lag = 0, while during El Niño, the high correlation resides mostly in the southwestern coastal regions and in California and Nevada (not shown). This also emphasizes that the presence of the different types of upper-level wave breaking events during different phases of ENSO is highly relevant for controlling the location and intensity of the precipitation over the western United States. Of further note, the correlation of precipitation with the lower-level PV (600–850 hPa) is very small (not shown). Outside these regions, for example, the regions over 30° – 45° N, 110° – 90° W, where there are few PV intrusion events, the correlation both between upper-level PV and precipitation and the upper-level PV and RH is low, indicating that precipitation fluctuations are not closely linked with PV fluctuations in these regions. The low correlation in these regions could also be due to the larger impact of measurement noise on precipitation, but the similar results are obtained using Tropical

Rainfall Measuring Mission data, confirming our findings (not shown).

5. Meridional water vapor transport

a. Meridional eddy flux diagnostics

Figures 1 and 2 show that the background large-scale mean flow provides important conditions for generating the different types of Rossby wave breaking. This raises a question about the role of transient eddies in maintaining or destroying the mean flow associated with anticyclonic or cyclonic Rossby wave breaking. Stone et al. (1999) noted that the life cycle of extratropical waves consists of baroclinic growth with poleward momentum fluxes. The upper-level eddy horizontal momentum flux and the lower-level eddy heat flux are known to be important components of the localized Eliassen–Palm flux, which is an indicator of the eddy activity flux, and the impact of eddies on the zonal mean basic flow (Trenberth 1986; Shapiro et al. 2001). Therefore, we use the horizontal eddy momentum flux

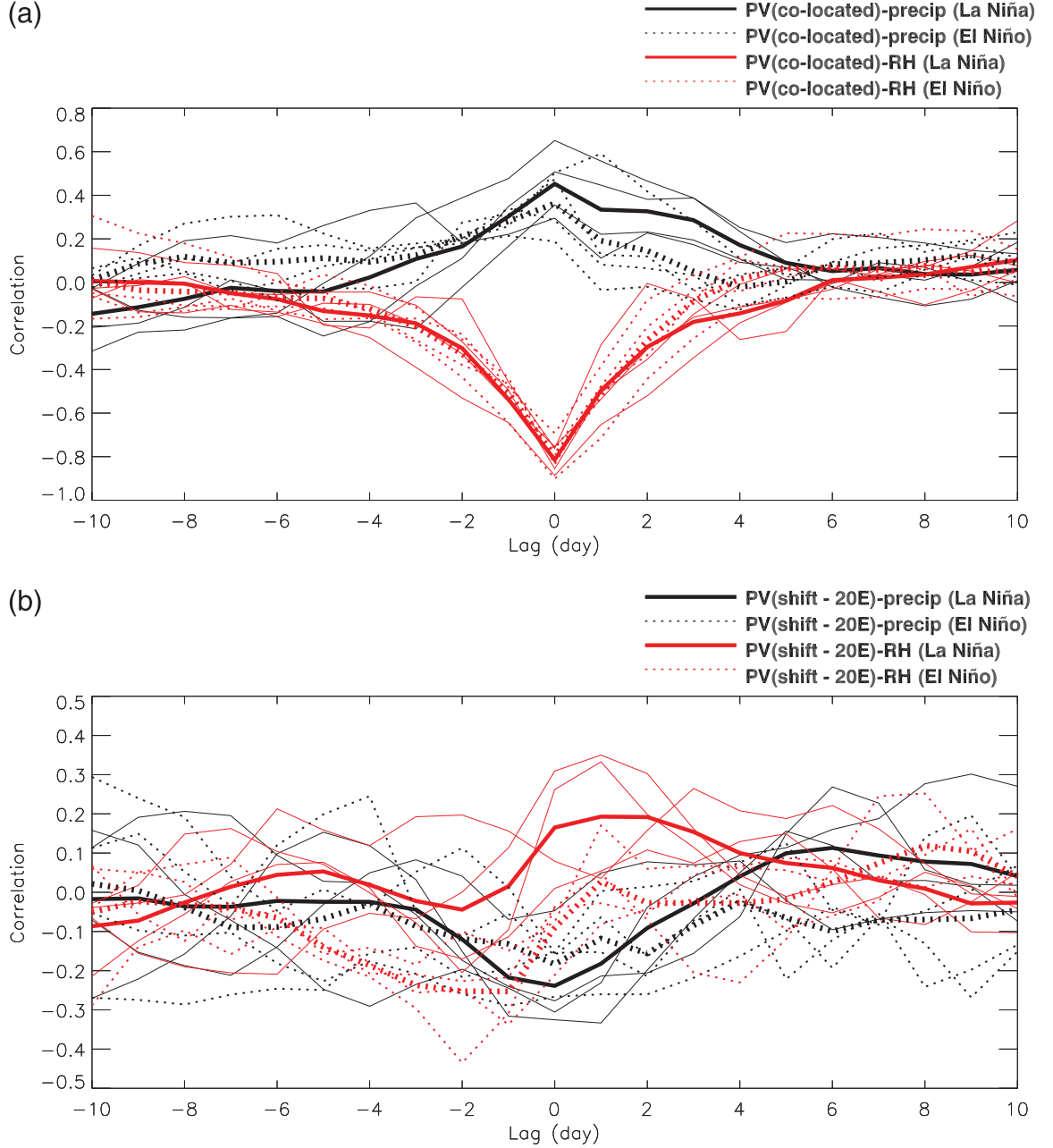


FIG. 8. (a) Lag correlation between PV at 250 hPa and precipitation over the regions in Fig. 7 (30° – 45° N, 130° – 110° W) (black) and between PV and collocated RH (red). (b) Lag correlations between PV at 250 hPa shifted to the west by 20° (30° – 45° N, 150° – 130° W) and precipitation (30° – 45° N, 130° – 110° W) (black), and between PV (20° – 35° N, 150° – 130° W) and RH (20° – 35° N, 130° – 110° W) (red). The solid and dashed lines respectively represent correlations for the four La Niña and the four El Niño years; thick lines are their means.

and the eddy heat flux as an indicator for the effect of the transient eddies on the local zonal flow.

Figures 9 and 10 provide insight to the characteristics of the horizontal momentum fluxes ($\bar{u}'v'$) and meridional heat fluxes ($\bar{v}'\theta'$) of the transient eddies, and their convergences averaged over 200° – 220° E, where ($\bar{\cdot}$) denotes time average during the NH winters. During La

Niña, a maximum of $\bar{u}'v'$ is found at around 250–300 hPa between 15° and 25° N. Two maxima of $\bar{u}'v'$ (double jet structure) are found for the individual La Niña winters (1998/99, 2000/01, 2007/08 and 2008/09), especially during the January–February time mean (not shown), but these features are smoothed out in the composite mean (Fig. 9a). This may be due to the variation of locations of

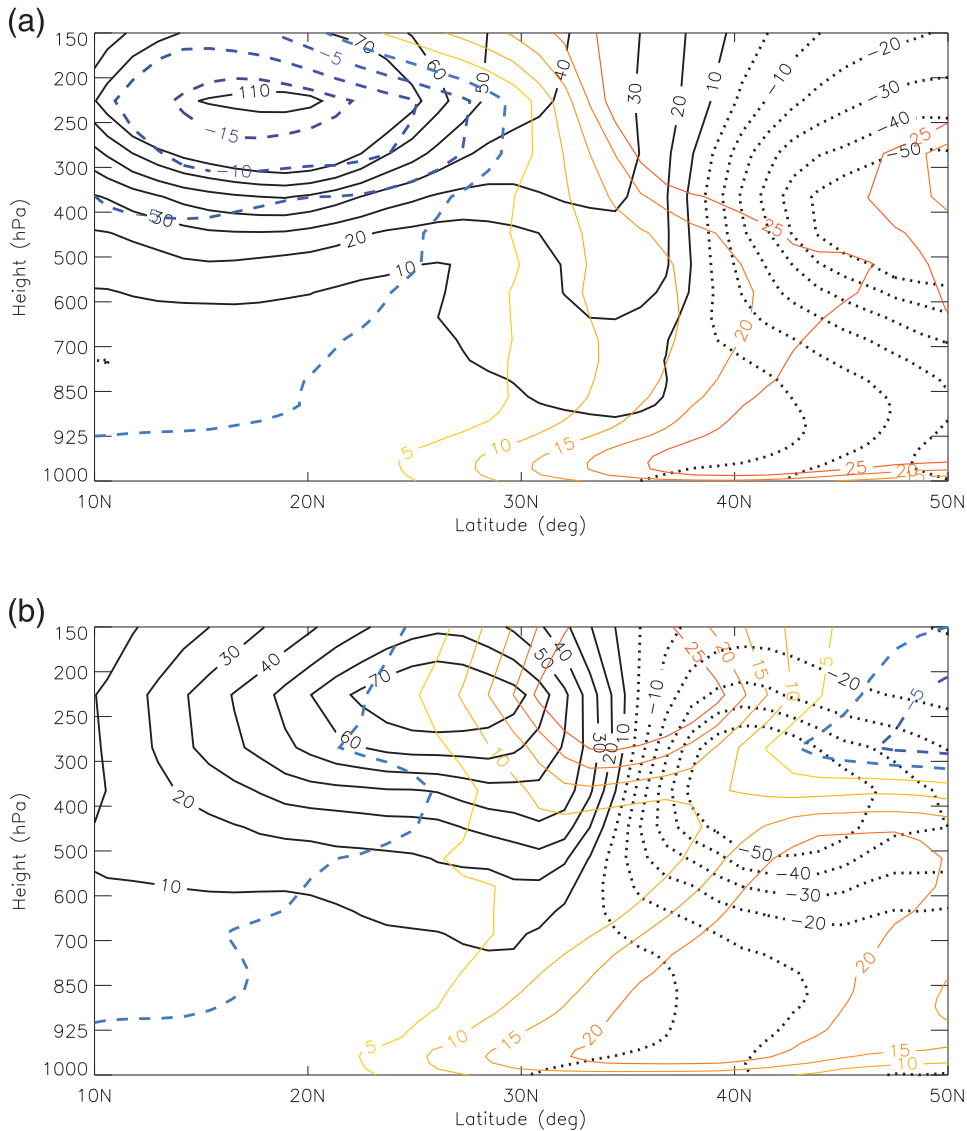


FIG. 9. The NH winter (DJF) latitude–height cross sections of the eddy momentum fluxes (black; $\text{m}^2 \text{s}^{-2}$) and eddy heat fluxes (color; increments of 5 K m s^{-1}) averaged over $160^\circ\text{--}140^\circ\text{W}$ in (a) the four La Niña and (b) the four El Niño years. Dashed lines indicate negative values.

winds during La Niña years. As shown in Fig. 1, the subtropical jet ($\sim 25^\circ\text{N}$) becomes weaker around 160°W and splits poleward and equatorward. The transient eddies play a role here by creating the double jet structures, which drive the eddy-driven jet poleward ($\sim 45^\circ\text{N}$). The La Niña composite shows that the convergence of the eddy momentum fluxes [$-\nabla \cdot (\overline{u'v'})$] and meridional eddy heat fluxes [$-\nabla \cdot (v'\theta')$] over these regions provides evidence for the role of transient eddies on the double jet structure and its interaction (Fig. 10a). The subtropical jet is counteracted by deceleration due to the divergence of the eddy momentum fluxes, which

acts to displace the subtropical jet poleward from its position (Held and Hou 1980; Lee and Kim 2003). Over $35^\circ\text{--}45^\circ\text{N}$, the convergence of the eddy momentum fluxes helps the eddy-driven jet to be maintained (Fig. 10a). Meanwhile, only a single maximum in momentum fluxes (a single jet structure) at 250 hPa is found during El Niño (Fig. 9b). This feature is also well observed in El Niño composite with a strong convergence of eddy momentum fluxes near $30^\circ\text{--}40^\circ\text{N}$, which is consistent with the fact that there is no shift in the jet poleward, but there is merging southward (Fig. 10b). Wave breaking regimes are substantially tied to the

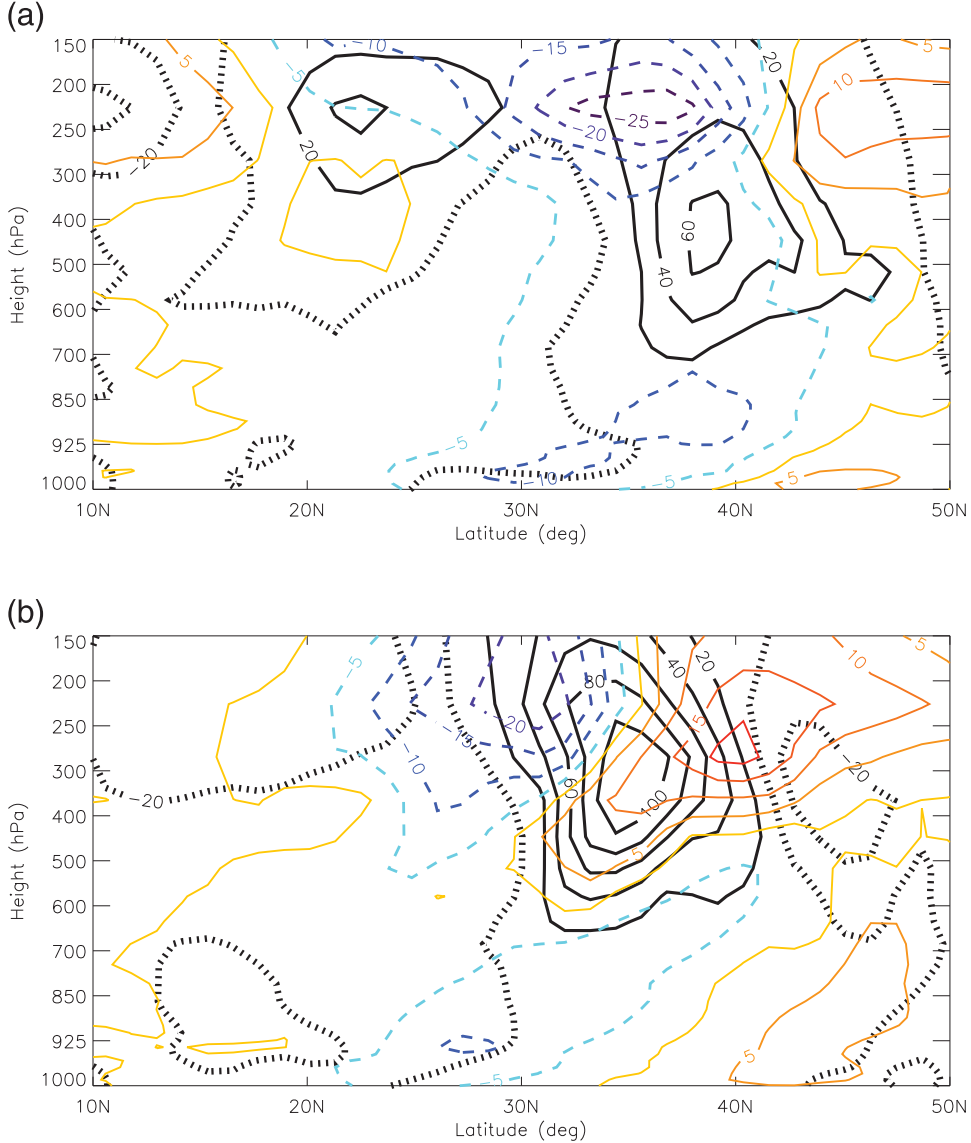


FIG. 10. As in Fig. 9, but for transient eddy momentum flux convergence (black solid; $\times 10 \text{ m s}^{-2}$) and transient eddy heat flux convergence (color solid; $\times 10 \text{ K s}^{-1}$). Broken black/dashed color lines indicate divergence.

movement of the equatorward (or poleward) $\overline{u'v'}$, as is the location of the jet. It is shown that the transient eddies associated with baroclinic waves such as LC1 and LC2 decelerate (accelerate) the jet due to the divergence (convergence) of $\overline{u'v'}$. Stronger westerly acceleration in the tropics means that $\overline{u'v'}$ will not be as effective in displacing the jet poleward (Chang 1995); hence, the jet position and westerly acceleration are more equatorward when compared to that in the weak westerly condition like during La Niña. In addition, during La Niña, eddy heat flux convergence (heating) resides next to the region of one of the local maxima

($\sim 4^\circ\text{N}$) of eddy momentum flux convergence, confined to the region of $40^\circ\text{--}50^\circ\text{N}$. In contrast, during El Niño, the eddy heat flux convergence in the upper levels occurs at the east side of eddy momentum flux convergence and decreases with height.

b. Relative contributions by transient eddies to water vapor transport

To evaluate the relative contribution of transient eddies to water vapor flux, we divide the vertically integrated water vapor meridional flux into time-mean and transient eddy components. As can be inferred from

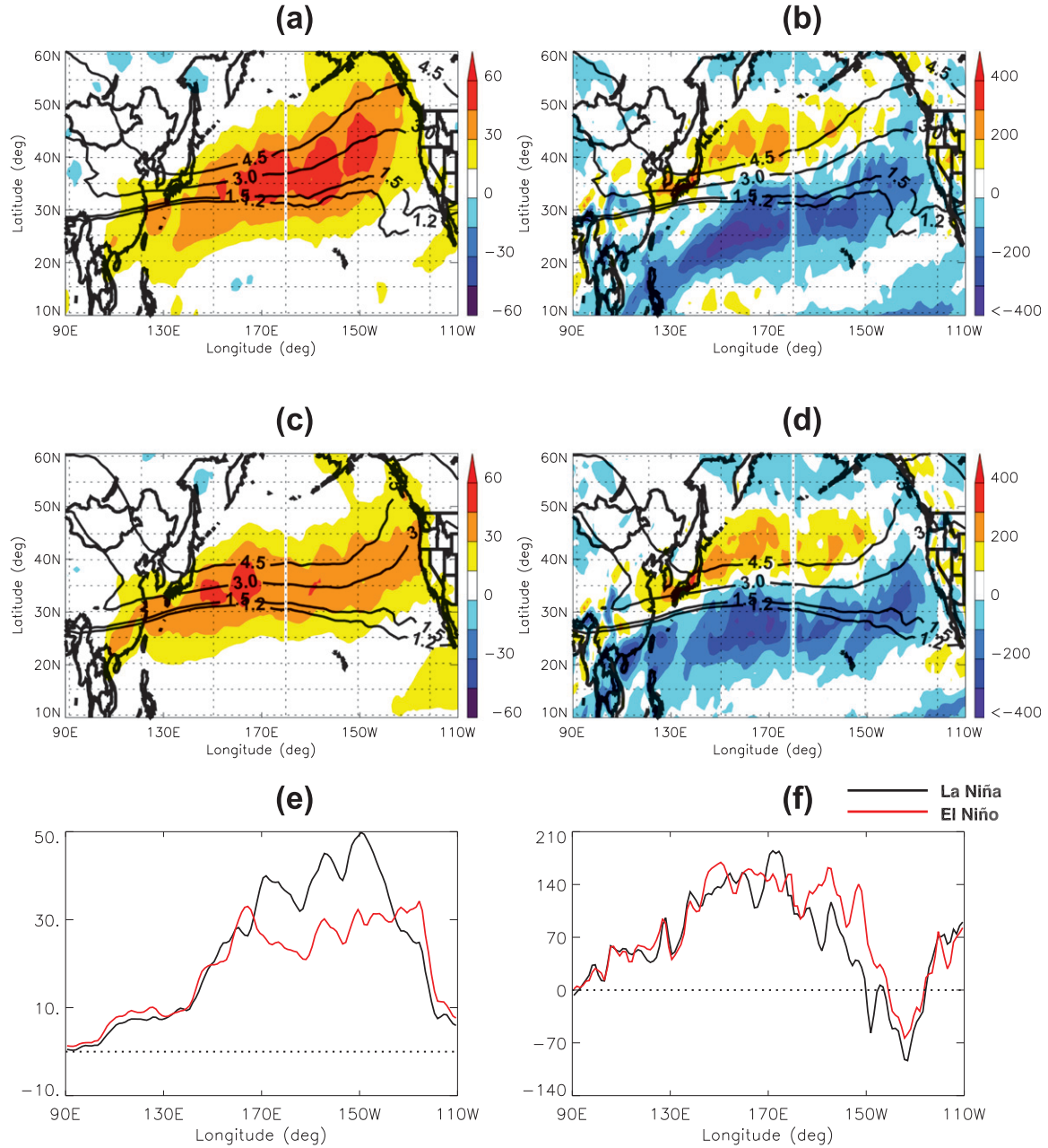


FIG. 11. The distributions of the vertically integrated (a),(c) meridional water vapor transport ($\bar{q}'v'$; $\text{kg m}^{-1} \text{s}^{-1}$) and (b),(d) latent heat flux convergence [$-L\bar{V} \cdot (\bar{q}'U')$, where $U = (u, v)$; W m^{-2}] by transient eddies during NH winter (DJF) in (top) the four La Niña and (middle) the four El Niño years over the Pacific basin. The black overlaid contours are the composite PV at 250 hPa. The positive (negative) values represent convergence (divergence). (e),(f) The values averaged over 35° – 50° N from (a),(c) and (b),(d), respectively.

Fig. 3, water vapor is largely transported by the mean flow (Trenberth et al. 2011; Newman et al. 2012). From north of 25°N , however, water vapor transport by the mean advection in La Niña is smaller than that of El Niño, with a noticeable increase in the role of transient eddies in transporting water vapor, particularly around 35° – 45°N (not shown). These results indicate that there is a significant contribution not only by the mean advection

but also by the transient eddies to the water vapor transport in the different phases of ENSO.

To see where water vapor is transported and accumulated by the transient eddies at the western United States in more detail, we calculate the vertically integrated meridional water vapor flux ($\bar{q}'v'$) and latent heat flux convergence [$-L\bar{V} \cdot (\bar{q}'U')$], where $U = (u, v)$ over the Pacific basin during ENSO years (Fig. 11).

The most notable feature is that meridional water vapor transport (Figs. 11a,c) and latent heat flux convergence (Figs. 11b,d) patterns differ, based on the location of the upper-level PV intrusions. During La Niña, moisture transport is mainly poleward by the transient eddies, especially from the edge of the PV intrusions [regions where anticyclonic wave breaking occurs (150°W , and 130°W at $25^{\circ}\text{--}50^{\circ}\text{N}$; Figs. 11a,e), or where there is latent heat flux divergence ($15^{\circ}\text{--}35^{\circ}\text{N}$, $150^{\circ}\text{--}170^{\circ}\text{E}$ and $15^{\circ}\text{--}40^{\circ}\text{N}$, $170^{\circ}\text{--}150^{\circ}\text{W}$; Fig. 11b)]. However, during El Niño, horizontal moisture transport is more dominant than its poleward transport (Fig. 11c) with divergence near the central Pacific ($15^{\circ}\text{--}30^{\circ}\text{N}$, $150^{\circ}\text{--}180^{\circ}\text{E}$) and the west coast of the United States ($130^{\circ}\text{--}120^{\circ}\text{W}$) (Fig. 11d).

Along the PV intrusions into the subtropics/midlatitudes (anticyclonic wave breaking) and into the northern Pacific in the high latitudes (cyclonic wave breaking), there is a reversal in the direction of the latent heat flux, resulting in more divergence (cooling) in the north and convergence (heating) in the south, indicating a contribution of the transient eddies to the northward heat transport (Figs. 11e,f). Although poleward heat transport by transient eddies is stronger in La Niña, the sum of eastward and poleward heat transport by transient eddies in El Niño is comparable to or higher than in the Pacific Northwest and along the coast of the western United States, especially at the region where cyclonic wave breaking and surface cyclones occur ($35^{\circ}\text{--}50^{\circ}\text{N}$, $150^{\circ}\text{--}130^{\circ}\text{W}$) (Figs. 3b and 11d). This suggests a large contribution of horizontal moisture transport due to transient eddies near the coastal regions of the United States during El Niño (Fig. 11f).

The behavior of transient latent heat flux divergence and/or convergence resembles the moisture transport patterns, which move moisture poleward and northward at the edge of PV intrusions. This is an indication that transient eddies play an important role in transporting moisture associated with latent heating from the tropics into the extratropics and the west coast of the United States, and that much of the transport from ocean to land occurs by transients, as shown by Newman et al. (2012). Observations show that narrow and long bands of moisture plumes, often referred to as atmospheric rivers (Ralph et al. 2004; Newman et al. 2012), carry much of the moisture from the tropics into the mid-latitudes, causing heavy rainfall on the west coast of the United States. These are often developed in association with equatorward filaments of extratropical cyclones in a baroclinic wave system, and they are one primary form of the moisture transport by the transient eddies associated with large-scale dynamics and wave breaking regimes.

c. Total water vapor fluxes and precipitable water

Figure 12 shows the total precipitable water [defined as $(1/g) \int_{p_0}^{p_1} \bar{q} dp$] and vertically integrated water vapor fluxes—defined as $(1/g) \int_{p_0}^{p_1} \bar{qv} dp$, where q is a specific humidity, v is a meridional wind component, $\bar{\cdot}$ denotes mean values within each adjacent pressure layer (dp), g is a gravitational constant, $p_0 = 1000 \text{ hPa}$, and $p_1 = 150 \text{ hPa}$ —in La Niña and El Niño years. The precipitable water and the total water vapor fluxes clearly describe the difference of moisture flux coming into the western United States during ENSO. The water vapor fluxes (maximum along the west coast of the United States is $141 \text{ kg m}^{-1} \text{ s}^{-1}$ and maximum over the ocean is $477 \text{ kg m}^{-1} \text{ s}^{-1}$) are also closely related to the enhanced surface anticyclones ($20^{\circ}\text{--}45^{\circ}\text{N}$, $170^{\circ}\text{--}130^{\circ}\text{W}$) associated with the LC1-like anticyclonic Rossby wave breaking during La Niña (see Figs. 11a and 12a). In contrast, the elongated water vapor flux (maximum along the coast is $186 \text{ kg m}^{-1} \text{ s}^{-1}$ and maximum over the ocean is $398 \text{ kg m}^{-1} \text{ s}^{-1}$) during El Niño reflects the presence of a strong subtropical jet in conjunction with the developing surface cyclones associated with the LC2-like cyclonic Rossby wave breaking on the northern branch of the jet. The difference of precipitable water and water vapor fluxes between El Niño and La Niña demonstrates that the western United States has more precipitable water ($\sim 4 \text{ kg m}^{-2}$) and water vapor flux ($\sim 70 \text{ kg m}^{-1} \text{ s}^{-1}$) into the coastal regions of the western United States during El Niño conditions than during La Niña conditions (Fig. 12c). This may be mainly due to the transport of moisture by the mean flow, combined with the contribution of the moisture transport by the transient eddies as shown in Fig. 11. These results show that different patterns in the water vapor transport provide important information in determining the location and intensity of precipitation on the western United States associated with the different phases of ENSO.

d. Moist static energy

In the previous sections, we have shown the patterns of winds, temperature, and meridional transport of water vapor and precipitable water during ENSO years. The winds, surface temperature, or meridional transport of water vapor itself can be used to describe the different atmospheric conditions during ENSO. However, these can only determine the air parcel's status or partially measure the amount of moisture content in the atmosphere; they cannot fully measure the total atmospheric energy content. The moist static energy (MSE) is potentially a more comprehensive variable for the analysis of atmospheric heat and moisture content as it represents the energy content (Neelin and Held 1987;

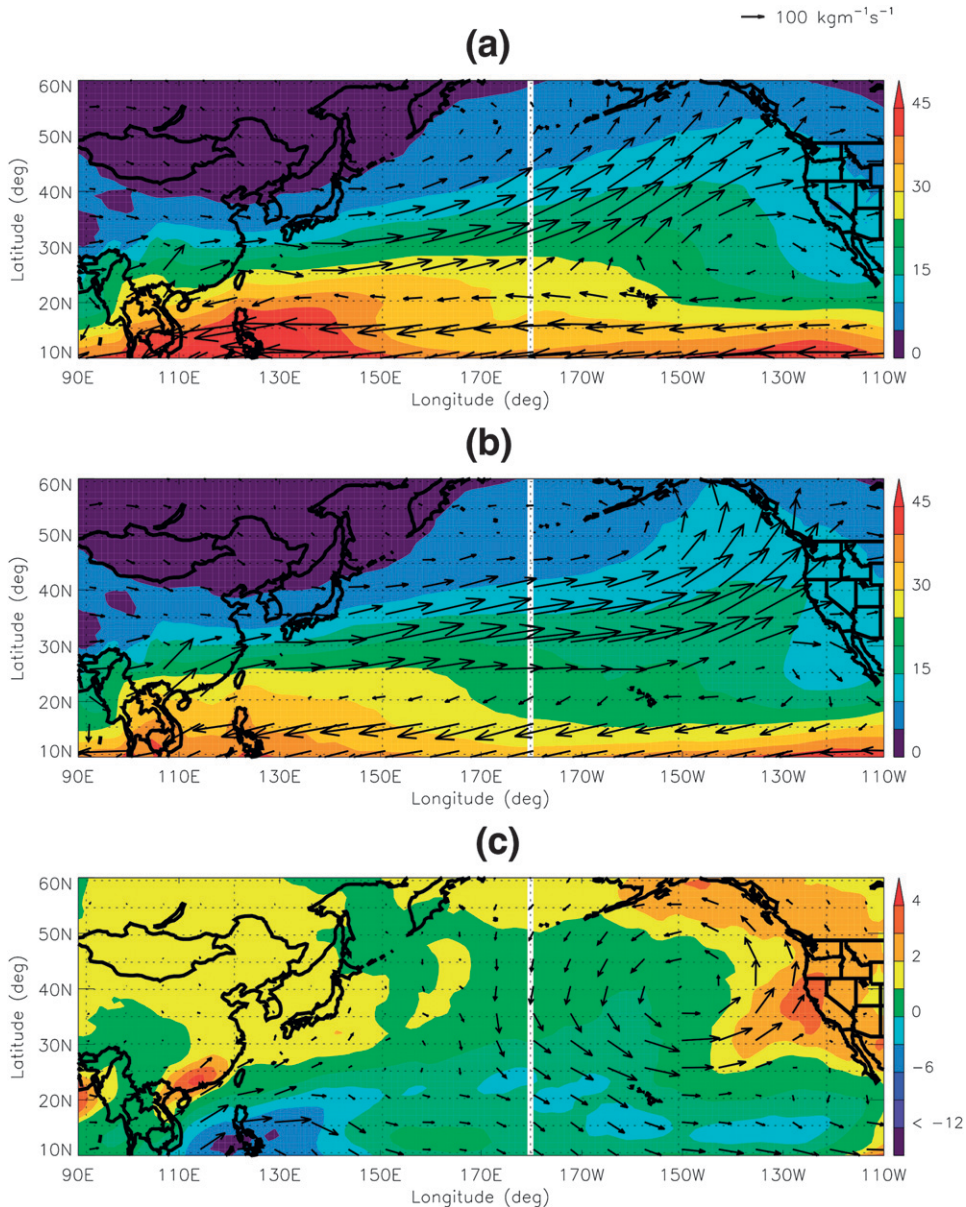


FIG. 12. The NH winter (DJF) vertically integrated precipitable water (shading; kg m^{-2}) and water vapor fluxes (arrows; $\text{kg m}^{-1} \text{s}^{-1}$) in (a) the four La Niña and (b) the four El Niño years; (c) the difference (b)–(a).

Pielke et al. 2004). Here we focus on the MSE (h), defined as

$$h = c_p T + Lq + gz,$$

where $c_p = 1004 \text{ J kg}^{-1} \text{ K}^{-1}$, T is temperature, L is the latent heat of vaporization ($2.5 \times 10^6 \text{ J kg}^{-1}$), and z is a geopotential height (Peixoto and Oort 1992). Figure 13 shows the vertically integrated meridional MSE flux [$hu = (C_p T + Lq + gz)u$] and zonal MSE flux

[$hv = (C_p T + Lq + gz)v$], where u and v are zonal and meridional wind, and MSE anomalies (subtracting from the zonal mean) during La Niña and El Niño. During La Niña, meridional MSE fluxes are high to the east of the PV intrusions (anticyclonic Rossby wave breaking), along with precipitable water and water vapor flux peaking near the central-north Pacific ($25^\circ\text{--}50^\circ\text{N}$, $160^\circ\text{--}140^\circ\text{W}$) (Fig. 13a). High meridional MSE flux are also found in $10^\circ\text{--}30^\circ\text{N}$, $130^\circ\text{--}110^\circ\text{E}$ on the east side of strong PV intrusion (anticyclonic Rossby wave breaking). These

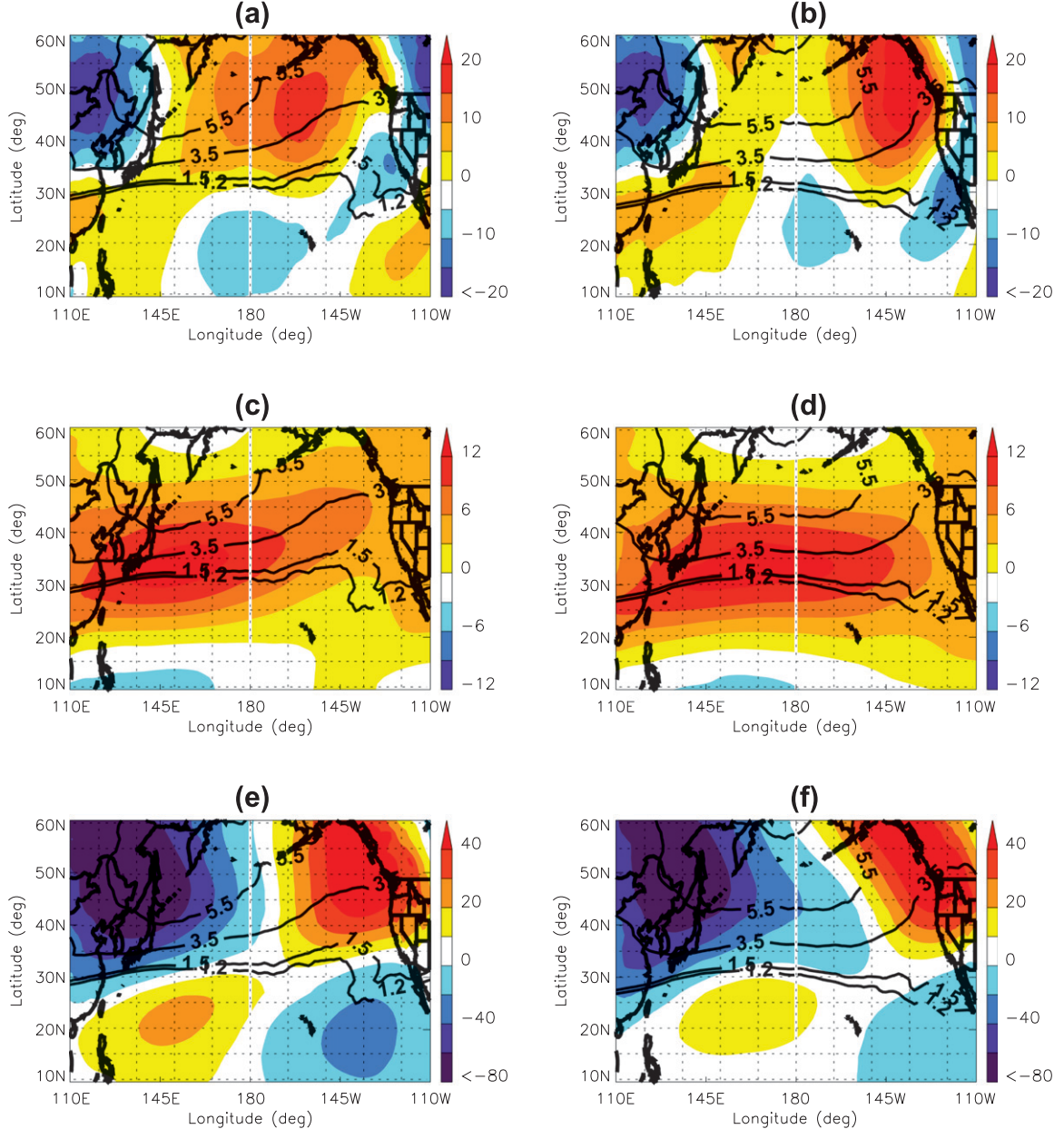


FIG. 13. The NH winter (DJF) vertically integrated total (a),(b) meridional and (c),(d) zonal moist static energy flux ($\times 10^9 \text{ W m}^{-2}$) and (e), (f) moist static energy anomalies (departures from the zonal mean; MJ kg^{-1}) in (left) the four La Niña and (right) the four El Niño years over the Pacific basin. The black overlaid contours are the composite PV (PVU) at 250 hPa.

appear to be primarily associated with the dynamics of upper-level PV intrusions which bring high moisture ahead of it, resulting in advection of warm air (high MSE) there. In contrast, during El Niño, strong positive meridional MSE fluxes are observed over the relatively confined regions in the eastern Pacific and along the west coast of the United States associated with cyclonic wave breaking (Fig. 13b). The zonal MSE flux between

La Niña and El Niño also shows the different patterns: more zonal variation of MSE flux during El Niño and more poleward variation of MSE flux with respect to PV intrusion (anticyclonic Rossby wave breaking) during La Niña (Figs. 13c,d). Both meridional and zonal MSE flux show a consistent pattern with vertically integrated water vapor and wind fields, and this indicates that MSE appears to be primarily regulated by water

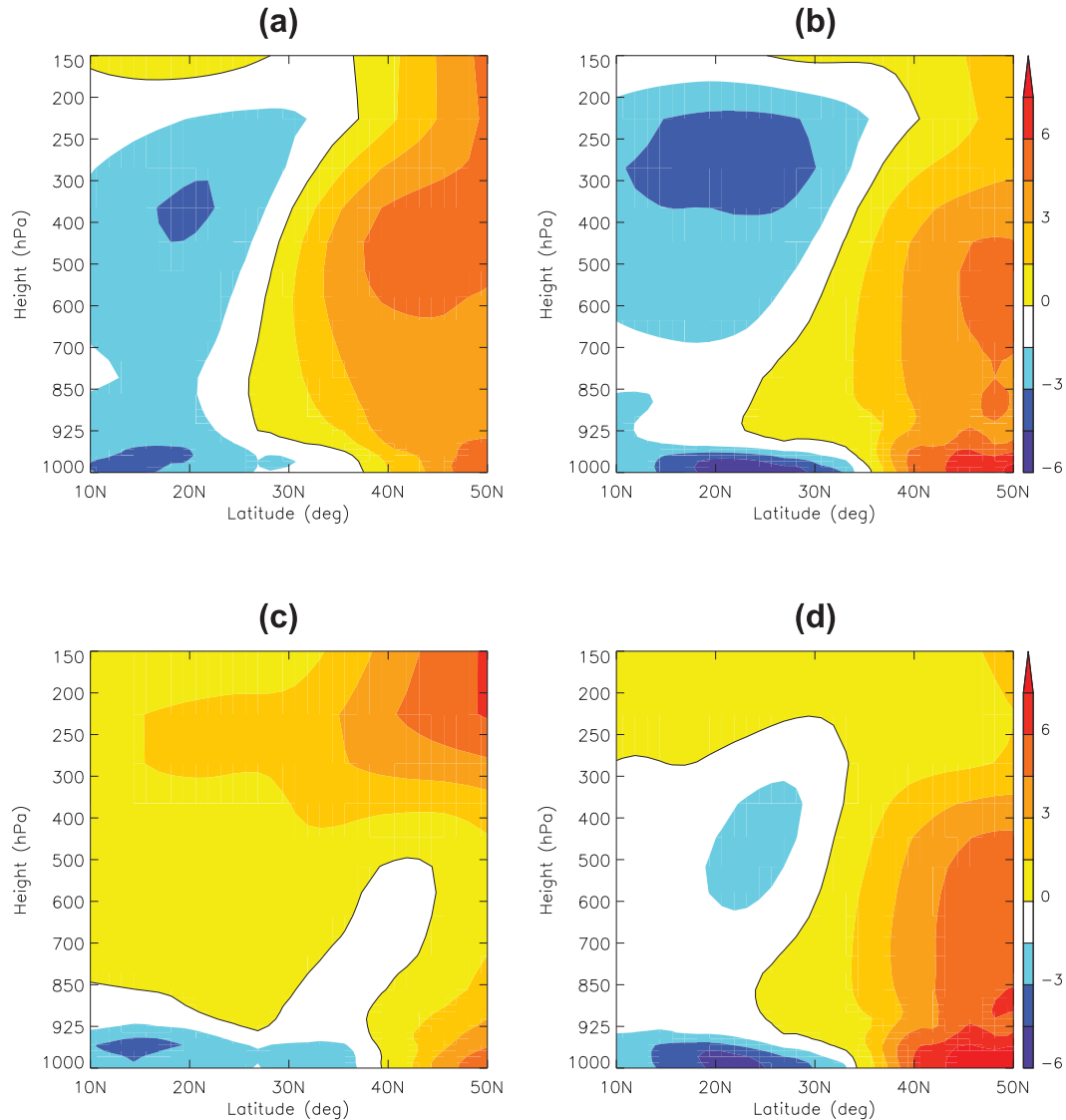


FIG. 14. The NH winter (DJF) latitude–height cross sections of moist static energy anomalies (departures from the zonal mean; $\times 10^{-1} \text{ MJ kg}^{-1}$) averaged over (a),(c) $160^{\circ}\text{--}140^{\circ}\text{W}$ and (b),(d) $130^{\circ}\text{--}110^{\circ}\text{W}$ in (top) the four La Niña and (bottom) the four El Niño years. The black contour represents a zero value.

vapor and the wind-driven components associated with different types of wave breaking (Figs. 12a,b and 13a–d). Large positive MSE anomalies are located near the central northern Pacific ($30^{\circ}\text{--}60^{\circ}\text{N}$, $160^{\circ}\text{--}120^{\circ}\text{W}$) during La Niña, whereas they are located on the confined regions of the eastern Pacific ($40^{\circ}\text{--}60^{\circ}\text{N}$, $140^{\circ}\text{--}110^{\circ}\text{W}$) during El Niño (Figs. 13e,f).

To better compare how much MSE anomalies (departure from the zonal mean) change between La Niña and El Niño depending on the presence of Rossby wave breaking events with altitude, we illustrate the latitudinal MSE anomalies with respect to the height averaged over $160^{\circ}\text{--}140^{\circ}\text{W}$ and $130^{\circ}\text{--}110^{\circ}\text{W}$ in Fig. 14. In both La Niña

and El Niño, MSE gradients are reversed around $30^{\circ}\text{--}40^{\circ}\text{N}$, which can be primarily seen as a result of MSE advection. Over $160^{\circ}\text{--}140^{\circ}\text{W}$, during La Niña, cold-air advection (low MSE anomalies) is not effective poleward but is effective upward, with high positive MSE anomalies extending to the subtropics ($\sim 25^{\circ}\text{N}$), the upper troposphere, and the lower stratosphere (around 200 hPa) (Fig. 14a). During El Niño, however, advection of the cold (low MSE anomalies) air pushes the high MSE anomalies poleward, leading to poleward movement of regions of ascending (or convective) motion, which is closely associated with high MSE anomalies (Maloney 2009) (Fig. 14c). Over $130^{\circ}\text{--}110^{\circ}\text{W}$, a transition in the

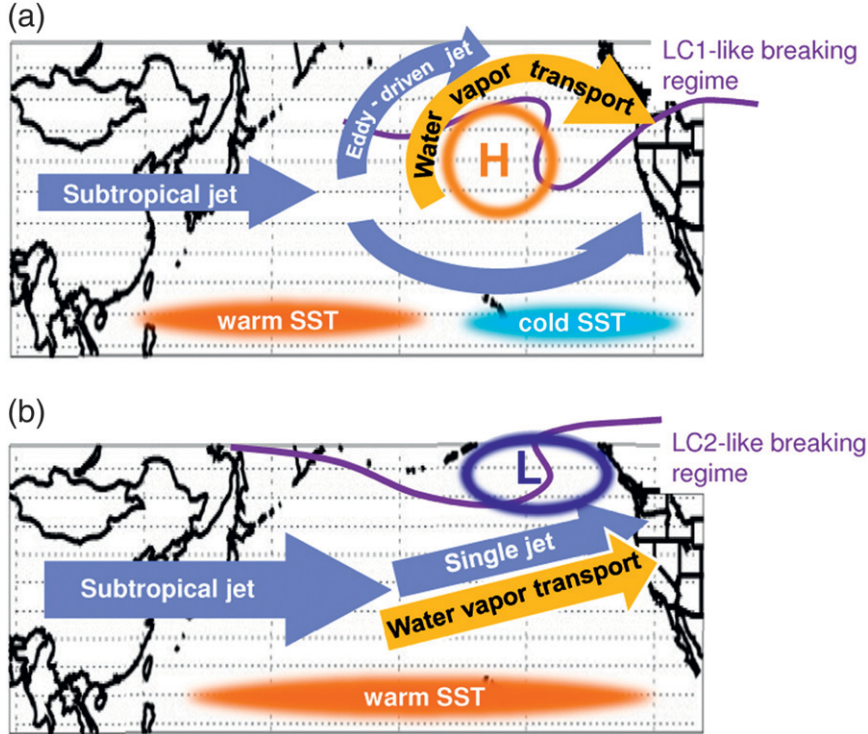


FIG. 15. Schematics of the characteristics of jet and moisture transport associated with the upper-level (a) anticyclonic Rossby wave breaking (LC1 like) in La Niña and (b) cyclonic Rossby wave breaking (LC2 like) in El Niño during NH winter (DJF). The size and the direction of blue arrows represent the magnitude and the direction of jet. The orange arrow represents the direction of moisture transport.

magnitude of high MSE anomalies occurs in the high latitudes (35° – 50° N). During La Niña, this appears to be associated with northward moisture transport into the North Pacific (Figs. 3a,c and 14b), whereas during El Niño it seems to be associated with developing surface cyclones together with the cyclonic wave breaking (Figs. 3b,d and 14d).

There are no strong positive MSE anomalies over 10° – 30° N, 130° – 110° W, on the east side of PV intrusion near the western United States (Fig. 13e). Although the maximum value of MSE anomaly is related to maximum water vapor transport, it cannot fully explain the characteristics of water vapor transport associated with wave breaking. This implies that MSE together with winds is useful to understand moisture transport associated with different wave breaking events. The transitions of meridional MSE fluxes and MSE anomalies between La Niña and El Niño show that maximum positive MSE anomalies tend to be located at regions of peak moisture content and ascending motions. This may suggest that they are closely controlled by the large-scale flows and location of PV intrusions associated with wave breaking regimes during the different phase of ENSO.

6. Summary and discussion

We have examined the precipitation characteristics over the western U.S. regions during ENSO years [four La Niña (1998/99, 2000/01, 2007/08, 2008/09) and four El Niño (1982/83, 1997/98, 2002/03, 2009/10) years] and related them to changes in Rossby wave breaking and moisture transport. The climatological patterns of the upper-level PV, wind, temperature, and geopotential height show significant differences between La Niña and El Niño. These lead to differences in the Rossby wave characteristics. During La Niña conditions the mid-Pacific subtropical jet is less zonal and weaker, leading to LC1-like anticyclonic wave breaking and strong PV intrusions into the subtropics. In contrast, the stronger jet during the El Niño conditions leads to LC2-like cyclonic wave breaking that prevents the upper-level PV from intruding into the subtropics. These two regimes are illustrated in Fig. 15.

The differences in Rossby wave breaking characteristics between ENSO phases give rise to different trajectory pathways, water vapor transport, and precipitation patterns and locations over the western United States.

During La Niña, trajectories originate in the eastern Pacific and move northeastward, and high water vapor is induced at the east edge of an anticyclonic wave breaking. In contrast, during El Niño trajectories originate in the subtropical western Pacific and propagate along a nearly zonal pathway, and eastward transport of moisture is enhanced along the surface cyclone accompanied by a cyclonic wave breaking.

In both phases, there are high correlations (up to 0.7) between upper-level PV and precipitation averaged over the Sierra Nevada and other regions along the west coast of the United States at lags from 0 to +1 day. At the same time lag (lag = 0 day), high correlation between upper-level PV and precipitation occurs in northern parts of the western United States during La Niña. In contrast, its peaks occur in the southern part of the western United States during El Niño at about lag = +1 day. This result demonstrates that the extreme precipitation events in the west coast regions of the United States during La Niña (El Niño) NH winters are related to the position and intensity of LC1-like anticyclonic Rossby wave breaking (LC2-like cyclonic Rossby wave breaking) events. The slight time lag of the maximum correlation between PV and precipitation in El Niño shows that the location and the intensity of the surface cyclones making landfalling precipitation may be sensitive to the change of the location of the LC2-like cyclonic Rossby wave breaking. Moore et al. (2010) observed that LC2 wave breaking mostly coexists with the surface cyclones, although a surface cyclone does not always accompany a wave breaking. However, the clear mechanism to explain the cause of the time lag between the location of the upper-level PV and the precipitation deserves further detailed investigation.

Transient eddies play a crucial role in modulating the jet and transporting the water vapor. The horizontal momentum flux convergence suggest that double jet structures exist during La Niña, while only a single jet exists during El Niño. Poleward moisture transport by the transient eddies by anticyclonic Rossby wave breaking during La Niña and zonal transport by the transient eddies by cyclonic Rossby wave breaking combined with surface cyclones during El Niño is more likely associated with the heavy precipitation over California and most of the west coast of the United States. The vertically integrated meridional moist static energy fluxes and MSE anomaly show that they are tied to moisture content, large-scale wind fields, and the vicinity of PV intrusion associated with the different regimes of the wave breaking during ENSO. High meridional MSE fluxes are found at the east side of anticyclonic wave breaking during La Niña and on the east side of cyclonic wave breaking during El Niño,

implying that advection of warm air (high MSE) and cold air (low MSE) may be regulated by the location of wave breaking regions.

There are a number of subsequent studies that would be suitable to build upon our results. First, it is necessary to recognize the linkage of Rossby wave breaking to the various weather regimes, especially in order to increase prediction skill of precipitation and extreme weather (e.g., blocking events) over the western United States. To do this, it is of primary importance to determine whether well-documented events for the extreme weather and precipitation (e.g., atmospheric rivers) can be represented in climate models or weather forecast models (Dettinger 2011; M. Wehner et al. 2012, personal communication; Kim et al. 2013; DeFlorio et al. 2013). Second, a more quantitative analysis using observational or idealized modeling studies is needed to resolve how much of the initial heat forcing (or thermal perturbation) will trigger the change of the mean flow and impact on the baroclinic waves to form the subtropical and eddy-driven jet. Third, for a given climate scenario such as ENSO or climate change, tracing the trajectories using the wind and diabatic heating data simulated from climate models (or idealized GCMs) will help to predict how the precipitation pattern will vary corresponding to variations of the wind and heating. This will enable us to explore how precipitation intensities, frequencies, and locations will change during ENSO or a varying climate. From this analysis, we may be able to understand the variability or changes in the precipitation patterns and predict them over the Sierra Nevada and the nearby western United States.

Acknowledgments. We give special thanks to Tapio Schneider for helping to improve the paper with insightful comments. We thank Bjorn Lambrightsen for his support and supervision. We also thank Inez Fung for helpful discussions and the anonymous reviewers for helpful comments. The research contributions from J.-M. Ryoo, D. E. Waliser, and E. J. Fetzer for this study were performed at Jet Propulsion Laboratory (JPL), California Institute of Technology (Caltech), under a contract with the National Aeronautics and Space Administration (NASA).

REFERENCES

- Anderson, J., F. Chung, M. Anderson, L. Brekke, D. Easton, M. Ejeta, R. Peterson, and R. Snyder, 2008: Progress on incorporating climate change into management of California's water resources. *Climatic Change*, **87** (Suppl. 1), 91–108, doi:10.1007/s10584-007-9353-1.
- Andrews, E. D., R. C. Antweiler, P. J. Neiman, and F. M. Ralph, 2003: Influence of ENSO on flood frequency along the California coast. *J. Climate*, **17**, 337–348.

- Aumann, H. H., and Coauthors, 2003: AIRS/AMSU/HSB on the Aqua mission: Design, science objectives and data products. *IEEE Trans. Geosci. Remote Sens.*, **41**, 253–264.
- Bjerknes, J., 1969: Atmospheric teleconnections from the equatorial Pacific. *Mon. Wea. Rev.*, **97**, 163–172.
- Bosilovich, M. G., J. Chen, F. R. Robertson, and R. F. Adler, 2008: Evaluation of global precipitation in reanalyses. *J. Appl. Meteor. Climatol.*, **47**, 2279–2299.
- , F. R. Robertson, J. Chen, 2011: Global energy and water budgets in MERRA. *J. Climate*, **24**, 5721–5739.
- Bradley, R. S., H. F. Diaz, G. N. Kiladis, and J. K. Eischeid, 1987: ENSO signal in continental temperature and precipitation records. *Nature*, **327**, 497–501.
- Carlson, T. N., 1980: Airflow through midlatitude cyclones and the comma cloud pattern. *Mon. Wea. Rev.*, **108**, 1498–1509.
- Chang, E. K. M., 1995: The influence of Hadley circulation intensity changes on extratropical climate in an idealized model. *J. Atmos. Sci.*, **52**, 2006–2024.
- Changnon, A., Ed., 2000: *El Niño 1997–1998: The Climate Event of the Century*. Oxford University Press, 232 pp.
- Davies, H. C., C. Schär, and H. Wernli, 1991: The palette of fronts and cyclones within a baroclinic wave development. *J. Atmos. Sci.*, **48**, 1666–1689.
- DeFlorio, M. J., D. W. Pierce, D. R. Cayan, and A. J. Miller, 2013: Western U.S. extreme precipitation events and their relation to ENSO and PDO in CCSM4. *J. Climate*, **26**, 4231–4243.
- Dettinger, M., 2011: Climate change, atmospheric rivers, and floods in California—A multimodel analysis of storm frequency and magnitude changes. *J. Amer. Water Resour. Assoc.*, **47**, 514–523, doi:10.1111/j.1752-1688.2011.00546.x.
- Diaz, H. F., and V. Markgraf, Eds., 1992: *El Niño: Historical and Paleoclimatic Aspects of the Southern Oscillation*. Cambridge University Press, 476 pp.
- Duchon, C. E., 1979: Lanczos filtering in one and two dimensions. *J. Appl. Meteor.*, **18**, 1016–1022.
- Fetzer, E., and Coauthors, 2003: AIRS/AMSU/HSB validation. *IEEE Trans. Geosci. Remote Sens.*, **41**, 418–431.
- Funatsu, B. M., and D. W. Waugh, 2008: Connections between potential vorticity intrusions and convection in the eastern tropical Pacific. *J. Atmos. Sci.*, **65**, 987–1002.
- Grubišić, V., R. Vellore, and A. Huggins, 2005: Quantitative precipitation forecasting of wintertime storms in the Sierra Nevada: Sensitivity to the microphysical parameterization and horizontal resolution. *Mon. Wea. Rev.*, **133**, 2834–2859.
- Held, I. M., and A. Y. Hou, 1980: Nonlinear axially symmetric circulations in a nearly inviscid atmosphere. *J. Atmos. Sci.*, **37**, 515–533.
- Higgins, R. W., J.-K. E. Schemm, W. Shi, and A. Leetmaa, 2000: Extreme precipitation events in the western United States related to tropical forcing. *J. Climate*, **13**, 793–820.
- Hoskins, B. J., and T. Ambrizzi, 1993: Rossby wave propagation on a realistic longitudinally varying flow. *J. Atmos. Sci.*, **50**, 1661–1671.
- , M. E. McIntyre, and A. W. Robertson, 1985: On the use and significance of isentropic potential vorticity maps. *Quart. J. Roy. Meteor. Soc.*, **111**, 877–946.
- Kalnay, E., and Coauthors, 1996: The NCEP/NCAR 40-Year Reanalysis Project. *Bull. Amer. Meteor. Soc.*, **77**, 437–471.
- Karoly, D. J., 1989: Southern Hemisphere circulation features associated with El Niño–Southern Oscillation events. *J. Climate*, **2**, 1239–1252.
- Kiladis, G. N., 1998: Observations of Rossby waves linked to convection over the eastern tropical Pacific. *J. Atmos. Sci.*, **55**, 321–339.
- , and K. M. Weickmann, 1992: Extratropical forcing of tropical Pacific convection during northern winter. *Mon. Wea. Rev.*, **120**, 1924–1938.
- Kim, J., 1997: Precipitation and snow budget over the southwestern United States during the 1994–1995 winter season in a mesoscale model simulation. *Water Resour. Res.*, **33**, 2831–2839.
- , D. E. Waliser, P. J. Neiman, B. Guan, J.-M. Ryoo, and G. A. Wick, 2013: Effects of land-falling atmospheric rivers on the cold season precipitation in California. *Climate Dyn.*, **40**, 465–474, doi:10.1007/s00382-012-1322-3.
- Knippertz, P., and J. E. Martin, 2007: A Pacific moisture conveyor belt and its relationship to a significant precipitation event in the semiarid southwestern United States. *Wea. Forecasting*, **22**, 125–144.
- Lee, S., and H.-K. Kim, 2003: The dynamical relationship between subtropical and eddy-driven jets. *J. Atmos. Sci.*, **60**, 1490–1503.
- L’Heureux, M. L., and D. W. J. Thompson, 2005: Observed relationships between the El Niño–Southern Oscillation and the extratropical zonal-mean circulation. *J. Climate*, **19**, 276–287.
- Maloney, E. D., 2009: The moist static energy budget of a composite tropical intraseasonal oscillation in a climate model. *J. Climate*, **22**, 711–729.
- Martius, O., C. Schwierz, and H. C. Davies, 2007: Breaking waves at the tropopause in the wintertime Northern Hemisphere: Climatological analyses of the orientation and the theoretical LC1/2 classification. *J. Atmos. Sci.*, **64**, 2576–2592.
- Matthew, A. J., and G. N. Kiladis, 1999: Interactions between ENSO, transient circulation, and tropical convection over the Pacific. *J. Climate*, **12**, 3062–3086.
- Michel, C., and G. Rivière, 2011: The link between Rossby wave breakings and weather regime transitions. *J. Atmos. Sci.*, **68**, 1730–1748.
- Mo, K. C., and W. Higgins, 1998: The Pacific–South American modes and tropical convection during the Southern Hemisphere winter. *Mon. Wea. Rev.*, **126**, 1581–1596.
- Moore, R. W., O. Martius, and T. Spengler, 2010: The modulation of the subtropical and extratropical atmosphere in the Pacific basin in response to the Madden–Julian oscillation. *Mon. Wea. Rev.*, **138**, 2761–2779.
- Neelin, J. D., and I. M. Held, 1987: Modeling tropical convergence based on the moist static energy budget. *Mon. Wea. Rev.*, **115**, 3–12.
- Neiman, P. J., F. M. Ralph, G. A. Wick, J. D. Lundquist, and M. D. Dettinger, 2008: Meteorological characteristics and overland precipitation impacts of atmospheric rivers affecting the west coast of North America based on eight years of SSM/I satellite observations. *J. Hydrometeorol.*, **9**, 22–47.
- Newman, M., G. N. Kiladis, K. M. Weickmann, F. M. Ralph, and P. D. Sardeshmukh, 2012: Relative contributions of synoptic and low-frequency eddies to time-mean atmospheric moisture transport, including the role of atmospheric rivers. *J. Climate*, **25**, 7341–7361.
- Orlanski, I., 2005: A new look at the Pacific storm track variability: Sensitivity to tropical SSTs and to upstream seeding. *J. Atmos. Sci.*, **62**, 1367–1390.
- Peixoto, J. P., and A. H. Oort, 1992: *Physics of Climate*. American Institute of Physics, 520 pp.
- Pielke, R. A., Sr., C. Davey, and J. Morgan, 2004: Assessing “global warming” with surface heat content. *Eos, Trans. Amer. Geophys. Union*, **85**, 210–211.

- Polvani, L. M., and J. G. Esler, 2007: Transport and mixing of chemical air masses in idealized baroclinic life cycles. *J. Geophys. Res.*, **112**, D23102, doi:10.1029/2007JD008555.
- Ralph, F. M., P. J. Neiman, and G. A. Wick, 2004: Satellite and CALJET aircraft observations of atmospheric rivers over the eastern North Pacific Ocean during the El Niño winter of 1997/98. *Mon. Wea. Rev.*, **132**, 1721–1745.
- , —, and R. Rotunno, 2005: Dropsonde observations in low-level jets over the northeastern Pacific Ocean from CALJET-1998 and PACJET-2001: Mean vertical-profile and atmospheric-river characteristics. *Mon. Wea. Rev.*, **133**, 889–910.
- , —, G. A. Wick, S. I. Gutman, M. D. Dettinger, D. R. Cayan, and A. B. White, 2006: Flooding on California's Russian River: The role of atmospheric rivers. *Geophys. Res. Lett.*, **33**, L13801, doi:10.1029/2006GL026689.
- Renwick, J. A., and J. M. Wallace, 1996: Relationships between North Pacific wintertime blocking, El Niño, and the PNA pattern. *Mon. Wea. Rev.*, **124**, 2071–2076.
- Rosen, R. D., D. A. Salstein, T. M. Eubanks, J. O. Dickey, and J. A. Steppe, 1984: An El Niño signal in atmospheric angular momentum and Earth rotation. *Science*, **225**, 411–414.
- Ryoo, J.-M., D. W. Waugh, and A. Gettelman, 2008: Variability of subtropical upper tropospheric humidity. *Atmos. Chem. Phys.*, **8**, 2643–2655.
- , J.-W. Kim, E. J. Fetzer, D. E. Waliser, 2010: A study of storm tracks and the cold season precipitation characteristics in California using trajectory model. *2010 Fall Meeting*, San Francisco, CA, Amer. Geophys. Union, Abstract A53B-0208.
- Schoeberl, M. R., and L. Sparling, 1995: Trajectory modeling. *Diagnostic Tools in Atmospheric Physics*, G. Fiocco and G. Visconti, Eds., Proceedings of the International School of Physics “Enrico Fermi,” Vol. 124, IOS Press, 289–306.
- Schubert, S. D., M. J. Suarez, P. J. Pegion, R. D. Koster, and J. T. Bacmeister, 2008: Potential predictability of long-term drought and pluvial conditions in the United States Great Plains. *J. Climate*, **21**, 802–816.
- Seager, R., N. Harnik, Y. Kushnir, W. Robinson, and J. A. Miller, 2003: Mechanisms of hemispherically symmetric climate variability. *J. Climate*, **16**, 2960–2978.
- Shapiro, M. A., and Coauthors, 1999: A planetary-scale to mesoscale perspective of the life cycles of extratropical cyclones: The bridge between theory and observations. *The Life Cycles of Extratropical Cyclones*, M. A. Shapiro and S. Grönås, Eds., Amer. Meteor. Soc., 139–185.
- , H. Wernli, N. A. Bond, and R. Langland, 2001: The influence of the 1997–99 El Niño–Southern Oscillation on extratropical baroclinic life cycles over the eastern North Pacific. *Quart. J. Roy. Meteor. Soc.*, **127**, 331–342.
- Simmons, A., S. Uppala, D. Dee, and S. Kobayashi, 2007: ERA-Interim: New ECMWF reanalysis products from 1989 onwards. *ECMWF Newsletter*, No. 110, ECMWF, Reading, United Kingdom, 1–53.
- Soong, S., and J. Kim, 1996: Simulation of a heavy wintertime precipitation event in California. *Climatic Change*, **32**, 55–77.
- Stone, E. M., W. J. Randel, and J. L. Stanford, 1999: Transport of passive tracers in baroclinic wave life cycles. *J. Atmos. Sci.*, **56**, 1364–1381.
- Suarez, M. J., Ed., 2008: The GEOS-5 Data Assimilation System—Documentation of versions 5.0.1, 5.1.0, and 5.2.0. NASA Tech Rep. NASA/TM-2008-104606, Vol. 27, 87 pp.
- Thorncroft, C. D., B. J. Hoskins, and M. E. McIntyre, 1993: Two paradigms of baroclinic-wave life-cycle behaviour. *Quart. J. Roy. Meteor. Soc.*, **119**, 17–55.
- Trenberth, K. E., 1986: An assessment of the impact of transient eddies on the zonal flow during a blocking episode using localized Eliassen–Palm flux diagnostics. *J. Atmos. Sci.*, **43**, 2070–2087.
- , J. T. Fasullo, and J. Mackaro, 2011: Atmospheric moisture transports from ocean to land and global energy flows in reanalyses. *J. Climate*, **24**, 4907–4924.
- Zipser, E., L. Stone, M. A. Cane, and H. Jarosh, 1994: El Niño chaos: Overlapping of resonances between the seasonal cycle and the Pacific Ocean–atmosphere oscillator. *Science*, **264**, 72–74.
- Waliser, D. E., and Coauthors, 2008: The “year” of tropical convection (May 2008–April 2010): Climate variability and weather highlights. *Bull. Amer. Meteor. Soc.*, **93**, 1189–1218.
- Waugh, D. W., 2005: Impact of potential vorticity intrusions on subtropical upper tropospheric humidity. *J. Geophys. Res.*, **110**, D11305, doi:10.1029/2004JD005664.
- , and L. M. Polvani, 2000: Climatology of intrusions into the tropical upper troposphere. *Geophys. Res. Lett.*, **27**, 3857–3860.
- , and Coauthors, 1994: Transport out of the lower stratospheric Arctic vortex by Rossby wave breaking. *J. Geophys. Res.*, **99**, 1071–1088.
- Webster, P. J., and J. R. Holton, 1982: Cross-equatorial response to middle-latitude forcing in a zonally varying basic state. *J. Atmos. Sci.*, **39**, 722–733.
- Wright, J. S., R. Fu, S. Fueglistaler, Y. S. Liu, and Y. Zhang, 2011: The influence of summertime convection over Southeast Asia on water vapor in the tropical stratosphere. *J. Geophys. Res.*, **116**, D12302, doi:10.1029/2010JD015416.
- Yanai, M., S. S. Esbensen, and J.-H. Chu, 1973: Determination of bulk properties of tropical cloud clusters from large-scale heat and moisture budgets. *J. Atmos. Sci.*, **30**, 611–627.